MASTERARBEIT | MASTER'S THESIS

Titel | Title

Metasediments of the Marina Basement Unit
on the Island Kos (Dodecanese, Greece)

verfasst von | submitted by

Michael Pichler BSc

angestrebter akademischer Grad | in partial fulfilment of the requirements for the degree of

Master of Science (MSc)

Wien | Vienna, 2025

Studienkennzahl lt. Studienblatt | Degree programme code as it appears on the student record sheet:	UA 066 815
Studienrichtung lt. Studienblatt | Degree programme as it appears on the student record sheet:	Masterstudium Erdwissenschaften
Betreut von | Supervisor:	Univ.-Prof. Mag. Dr. Bernhard Grasemann

I. Acknowledgments

First and foremost, I would like to thank you, my supervisor Bernhard Grasemann, for your support and advice in the realization of this thesis. Starting with the fieldwork on Kos under the mounting late summer heat on the slopes of Mount Dikeos you introduced me to the geological conditions.

This was followed by the analytical work at the University, where you gave me valuable input on microscopical, structural and tectonic aspects. Thank you, for giving me confidence and freedom and for always making time for me, even when you actually did not have any.

Thomas Griffiths, thank you for helping me with the microprobe work. Your support on all petrological issues was extremely beneficial. Big gratitude is expressed to Michl Bestmann for the assistance with the SEM work and his helpful inputs on microstructural aspects. Gerlinde Habler is greatly thanked for her expertise on microstructural and petrological aspects in the thin section microscopy. Great thanks are expressed to Gerd Rantitsch of the Technical University of Leoben for assisting me with the RSCM analyses and providing the processed data. Thank you for teaching me the preparation and analysis itself. I would like to thank the staff of the thin section lab, especially Claudia Beybel for preparing the polished thin sections. Theodoros Ntaflos's assistance at the electron microprobe is greatly acknowledged.

Elisabeth Fink is thanked for critical and constructive editing.

I would like to thank everyone in the Structural Processes Group for a very pleasant working environment and kind support.

Financial support from the Wolfgang Schollenberger foundation for the conducted microprobe work is gratefully acknowledged.

Finally, I would like to thank my family, friends and fellow students for supporting me all the way through my studies.

Acknowledgment of the usage of AI

Hereby, I confirm the usage of the AI tool Microsoft 365 Copilot (https://www.microsoft.com/de-de/microsoft-365-copilot) and deepl (https://www.deepl.com/de/translator) to support the refinement of academic wording, translation and the Phyton-based coding for the presented binary and ternary plots in the results chapter. I am familiar with the University guidelines on AI usage, and this thesis is in accordance with them.

II. Abstract

This study investigates the metamorphic and tectonic evolution of the Marina Basement Unit on the island of Kos (Dodecanese, Greece). Until recently, the deformation grade of the Marina Basement Unit has been underestimated. Detailed fieldwork, petrographic analysis, electron microprobe measurements, and Raman spectroscopy of carbonaceous material (RSCM) were employed to characterize mineral assemblages, deformation structures, and peak metamorphic temperature conditions.

Results indicate a poly-metamorphic history initiated by a Variscan regional metamorphic event under MP/MT conditions. This event is recorded by mylonitic foliation, Type 2 and Type 3 interference patterns, and pressure-dominated fabrics. RSCM thermometry indicates peak temperatures of 568–665 °C, suggesting a Barrovian amphibolite facies. The Paleozoic metasediments were overprinted by contact metamorphism within an aureole associated with the intrusion of a Miocene monzonite pluton. The contact aureole is distinguished by different hornfels facies. The innermost zone is defined by hornfels and skarn paragenesis containing andalusite, sillimanite, cordierite and wollastonite, which is restricted to within tens of meters away from the intrusion. Based on chiastolite relics the outer aureole probably ranges to about ~2,5 km. The host rock points out that a steep thermal gradient restricts the high temperature minerals near the pluton.

The chemistry of garnet porphyroblasts is dominated by almandine with minor pyrope and spessartine components, whereas an endoskarn garnet exhibits grossular and andradite enrichment. Zoning profiles display weak or absent growth zoning, suggesting compositional homogenization that obliterated former zoning. Decomposed porphyroblast structures and symplectitic textures indicate retrograde metamorphism following the Variscan prograde event. Some schists of the Marina Basement Unit contain an astonishing porosity and many fluid pathways. In proximity to the Paleocene Kos Thrust with top-to-N shear sense and the Oligocene Kos detachment with top-to-S shear sense, imposing additional structural overprints on the Marina Basement Unit.

III. Zusammenfassung

Diese Studie untersucht die metamorphe und tektonische Entwicklung der Marina Basement Einheit auf der Insel Kos (Dodekanesen, Griechenland). Bis vor Kurzem wurde der Deformationsgrad der Marina Basement Einheit unterschätzt. Detaillierte Geländearbeiten, petrographische Analysen, Elektronenmikrosondenmessungen und Raman-Spektroskopie von kohlenstoffhaltigem Material (RSCM) wurden eingesetzt, um Mineralassoziationen, Deformationsstrukturen und Bedingungen der maximalen Metamorphosetemperatur zu charakterisieren.

Die Ergebnisse weisen auf eine polymetamorphe Geschichte hin, welche mit einem variszischen regionalen Metamorphoseereignises unter mittlerem Druck und mittlerer Temperatur (MP/MT) begann. Dieses Ereignis ist durch mylonitische Foliation, Interferenzmuster vom Typ 2 und Typ 3 sowie druckdominierte Gefüge dokumentiert. Die RSCM-Thermometrie ergibt Spitzentemperaturen von 568-665 °C, was auf eine Barrow'sche Amphibolit-Fazies hinweist. Die paläozoischen Metasedimente wurden anschließend durch Kontaktmetamorphose innerhalb einer Aureole überprägt, die mit der Intrusion eines miozänen Monzonitplutons verbunden ist. Die Kontakt-Aureole ist durch unterschiedliche Hornfels-Fazies gekennzeichnet. Die innerste Zone, die sich innerhalb weniger Dutzend Meter vom Pluton befindet, wird durch Hornfels- und Skarnparagenesen mit Andalusit, Sillimanit, Cordierit und Wollastonit definiert. Basierend auf Chiastolithrelikten erstreckt sich die äußere Aureole vermutlich bis zu etwa 2,5 km. Das Wirtsgestein weist darauf hin, dass ein steiler thermischer Gradient die Hochtemperaturminerale auf den Bereich nahe dem Pluton beschränkt.

Die Chemie der Granatporphyroblasten wird von Almandin mit geringen Anteilen von Pyrop und Spessartin dominiert, während der Granat eines Endoskarns eine Anreicherung von Grossular und Andradit zeigt. Zonierungsprofile weisen eine schwache oder fehlende Wachstumszonierung auf, was auf eine chemische Homogenisierung hindeutet, die frühere Zonierungen ausgelöscht hat. Zerfallene Porphyroblaststrukturen und symplektitische Texturen deuten auf eine retrograde Metamorphose nach dem variszischen progradierenden Ereignis hin. Einige Schiefer der Marina Basement Einheit zeigen eine bemerkenswerte Porosität und zahlreiche Fluidwege. Schließlich wurden die Deformationsgefüge zusätzlich durch die Nähe zur paläozänen Kos Überschiebung mit einem Schersinn Top-nach-N und das oligozäne Kos Detachment mit einem Schersinn Top-nach-S überprägt, welche weitere strukturelle Überprägungen auf die Marina Basement Einheit ausübte.

IV. Nomenclature and abbreviations

group	endmember	abbrevation	composition
alumosilicate	andalusite	And	Al_2SiO_5
	fibrolite (fibrous sillimanite)	Fib	
	chiastolite	Chist	
amphibole	-	Amp	$A\ B_{3\text{-}5}\ C_2[OH, F)_2/Si_8O_{22}$
	hornblende	Hbl	$(Ca,Na,K)_{2\text{-}3}\ (Mg,Fe,Al)_5\ [(OH,F)_2\ /(Si,Al)_2Si_6O_{22}$
apatite	-	*Ap*	$Ca_5[F/(PO_4)_3]$
biotite	-	*Bt*	$K\ (Mg, Fe^{2+}, Mn^{2+})_3\ [(OH, F)_2\ \vert\ (Al, Fe^{3+}, Ti^{3+})\ Si_3O_{10}]$
carbonates	calcite	*Cal*	$CaCO_3$
	-	*Cb*	XCO_3
chlorite	-	Chl	$(Mg, Fe^{2+}, Al)_6[(OH)_8\vert AlSi_3O_{10}]$
clinopyroxene	-	*Cpx*	$(Na, Ca)\ (Fe^{2+}, Mg, Mn, Fe^{3+}, Al^{6+}, Ti^{4+})\ [(Al^{4+}, Si)_2O_6]$
garnet	pyrope	*Prp*	$Mg_3Al_2\ [SiO_4]_3$
	almandine	*Alm*	$Fe^{2+}{}_3Al_2\ [SiO_4]_3$
	spessartine	*Sps*	$Mn_3Al_2\ [SiO_4]_3$
	grossular	*Grs*	$Ca_3Al_2\ [SiO_4]_3$
	hydrogrossular	*Hgrs*	$Ca_3Al_2\ [X']_3$
	andradite	*Adr*	$Ca_3Fe_2\ [SiO_4]_3$
	Ti-andradite (Melanite)	X_{CaTi}	$Ca_3(Fe^{3+}, Ti^{3+})_2\ [SiO_4]_3$
	-	*Grt*	$(Ca, Fe^{2+}, Mn, Mg)_3\ (Al, Fe^{3+}, Cr^{3+}, Ti)_2\ [SiO_4]_3$
orthopyroxene	-	*Opx*	$(Mg, Fe)_2\ SiO_6$
plagioclase	-	*Pl*	$(Na, Ca)\ [(Al, Si)_2O_8]$
	albite	*Ab*	$Na\ [(Al, Si)_2O_8]$
	oligoklas	*Olg*	$(Na_{0.75}\ Ca_{0.25})\ (Si_{0.75}\ Al_{0.25})_4O_8$
scapolithe	-	*Scp*	$(Na,Ca)_4\ [(Cl, CO_3)\vert(Al, Si)_{12}O_{24}]$
pyroxene	orthopyroxene-clinopyroxene	*Px*	ab [(Si, Al)2O6]
white mica	-	Wmca	$K\ x\ [Si_4O_{10}(OH)_2]$
	cordierite	*Crd*	$(Mg, Fe)_2Al_3[AlSi_5O_{18}]$
	graphite	*Gr*	C
	ilmenite	*Ilm*	$FeTiO_3$
	limonite	*Lm*	$Fe\ (O\ \vert\ OH)_i$
	wollastonite	*Wo*	$CaSiO_3$

Common constituents amphibole: A = Na, Ca, Mg, Li; B = Fe^{3+}, Mg; C = Al, Fe^{3+}; Common constituents pyroxene: a = Na, Ca, Mg, Fe^{2+}, Mn b = Mg, Fe^{2+}, Mn, Fe^{3+}, Al, Ti, Cr; White mica constituents: x=Al_2, Al (Mg, Fe^{2+}), Fe^{3+} (Mg, Fe^{2+}), $Fe^{2+}{}_3$, $Mg^{2+}{}_3$, etc.; Carbonates common constituents: X=Ca, Mg, Fe, Pb, etc.; Hydrogrossular constituents: X´= SiO_4 gets substituted by OH

The nomenclature and abbreviations are based on (Warr, 2021), Whitney & Evans (2010) and constituents on Rösler, (1979) & Grew et al. (2013).

PPL	Parallel polarized light
XPL	Crossed polarized light
SEM	Scanning electron microscopy
EDX	Energy dispersive X-ray spectroscopy
EMPA	Electron microprobe analysis
RSCM	Raman spectroscopy of carbonaceous material
BSE	Backscattered electron
SPO	Shape preferred orientation
CPO	Crystallographic preferred orientation
SGR	Subgrain rotation
s	Schistosity planes
c’	Cleavage
sympl	Symplektite
f_i	Fold
fa_i	Fold axis
myl	Mylonite

Table of Content

1 Introduction & Statement of aim

The island of Kos is located in the eastern Mediterranean region and is one of the central Dodecanese islands (Fig.1). It is famous for the 161 ka Kos Plateau Tuff eruption, its vulcanism and the neotectonic history (e.g., Allen et al., 1999; Bachmann et al., 2019; Keller, 1969; Smith et al., 1996; Pe-Piper et al., 2005; Willmann, 1983). The eruption is the main source of vulcanoclastics and the largest Quaternary eruption from volcanic centers in the Aegean region, comparable to the Late Bronze Age Santorini eruption (Bachmann et al., 2019; Pe-Piper et al., 2005). This work, however, will highlight the Paleozoic metasediments of the Marina Basement Unit and its Miocene intrusion.

The tectonostratigraphic context, including its lithology and their certain age, varies and underlies a broad discussion. The exception is the monzonitic pluton that intruded into Paleozoic metasediments bordered by wildflysch in the west, which were later partly covered by Mesozoic to Eocene carbonates (limestone klippen) with a flysch layer on top (Altherr et al., 1976; Blondeau et al., 1975; Desio, 1931; Dürr & Jacobshagen, 1986). These are the basement units that crop out at the Dikeos massif (also known as Dicheo massif), located in the southeastern part of the island with the Mt. Dikeos (846 m) as its peak.

The Mesozoic limestone klippen, lower Cenozoic carbonates and the wildflysch are described to be either juxtaposed by a thrust (Altherr et al., 1976; D. Papanikolaou & Nomikou, 1998) or by a detachment fault (i.e., Kos Detachment; Van Hinsbergen & Boekhout, 2009). The Paleozoic metasediments were proposed to display a tectonic window that opened after the intrusion of the quartz monzonite by a suggested Kos Detachment with top-to-N kinematics (Van Hinsbergen & Boekhout, 2009). A tectonic contact between the Wildflysch and Paleozoic sediments was drawn (D. Papanikolaou & Nomikou, 1998) and later described to be part of the detachment (Van Hinsbergen & Boekhout, 2009). Mesozoic olistholits in the wildflysch are defined to lie above the late Cretaceous to Tertiary or Paleogene wildflysch (Dürr & Jacobshagen, 1986; D. Papanikolaou & Nomikou, 1998). The recent study of Roche et al. (2024) shows that the island of Kos belongs to the Pelagonian domain and its lithology can be correlated with the Units of the neighboring island Kalymnos. Although it is also related to the Anatolian domain in southwestern Turkey, the deformation history they share is still in dispute.

The basement geology of Kos in the Dikeos massif is represented by the Paleozoic Marina Basement Unit (Paleozoic metasediments), which was thrusted onto the Dikeos Unit (Paleozoic Unit and Permo-Triassic Wildflysch) during the Eocene. New age data shows that the Dikeos unit must be at least Triassic, and the supposed contact is stated to be a gradational depositional horizon. Therefore it is possible to unite them as the Dikeos Unit. Furthermore, the Mesozoic to Eocene Marina Cover Unit (former olistholites and limestone klippen) is juxtaposed on top of the Dikeos Unit along the Kos Detachment with a top-to-S shear sense, which was active in the Oligocene. The last stage was a Miocene intrusion of quartz monzonite, which penetrates the Marina Basement Unit and has a probable contact to the Marina Cover Unit that is eradicated by high-angle normal faults and thus could not be confirmed. (Roche et al., 2024)

Upper Miocene to Quaternary marine to lacustrine sediments, which are overlain by Pliocene to Pleistocene volcaniclastic deposits with isolated Mesozoic limestone blocks. These sediments cover about three quarter of the island surface (Dürr & Jacobshagen, 1986).

The influence of the metamorphic overprint on the Paleozoic sediments of the Marina Basement Unit in the area of the contact aureole, is well described and investigated by Altherr et al. (1976) and Kalt et al. (1998). The Marina Cover Unit on top indicates no contact metamorphic alteration (Altherr et al., 1976; Desio, 1931; Van Hinsbergen & Boekhout, 2009). The dominance of contact metamorphism that derived from the pluton which intruded at a depth of about 12 km at around 9 to 12 Ma ago was highlighted by Altherr et al. (1976), (1982) & Henjes-Kunst et al. (1988) & Kalt et al. (1998). At the surface the crystallin reveals an approximate outcrop diameter of ~4 km (Roche et al., 2024). A contact aureole was estimated by using common contact metamorphic minerals (Altherr et al., 1976). A map with isograds was created that depicts index minerals, which represent certain temperature levels or distances to the intrusion. With the study of Kalt et al. (1998), this map was extended; thin section descriptions including qualitative and quantitative composition data, as well as petrological analysis allowed the authors to deter temperatures and pressure conditions for elected samples near proposed isograds. But the temperature observations are to be questioned because thermometric calculations yield that the heating of the ambient host rock above 500° C is limited to a distance of <600 m from the contact (Roche et al., 2024). In the field exoskarns were only found close to the contact in a range of approximately up to 500 m and contact metamorphism exceeding this distance is doubtful.

This brings us to the aim of this work. The focus was to distinguish the Type of Metamorphism that was responsible for rock formation. As already mentioned, just the Marina Basement Unit is affected by that contact metamorphic overprint and itherefore the area of interest. In the areole area of the intrusion porphyroblasts of garnet and Plagioclase were examined for zoning. To verify the reliability of the given temperatures presented by Kalt et al. (1998), new temperature data proximal to the pluton were acquired. Based on the data gathered from this work, the deformation history of the Marina Basement Unit was set.

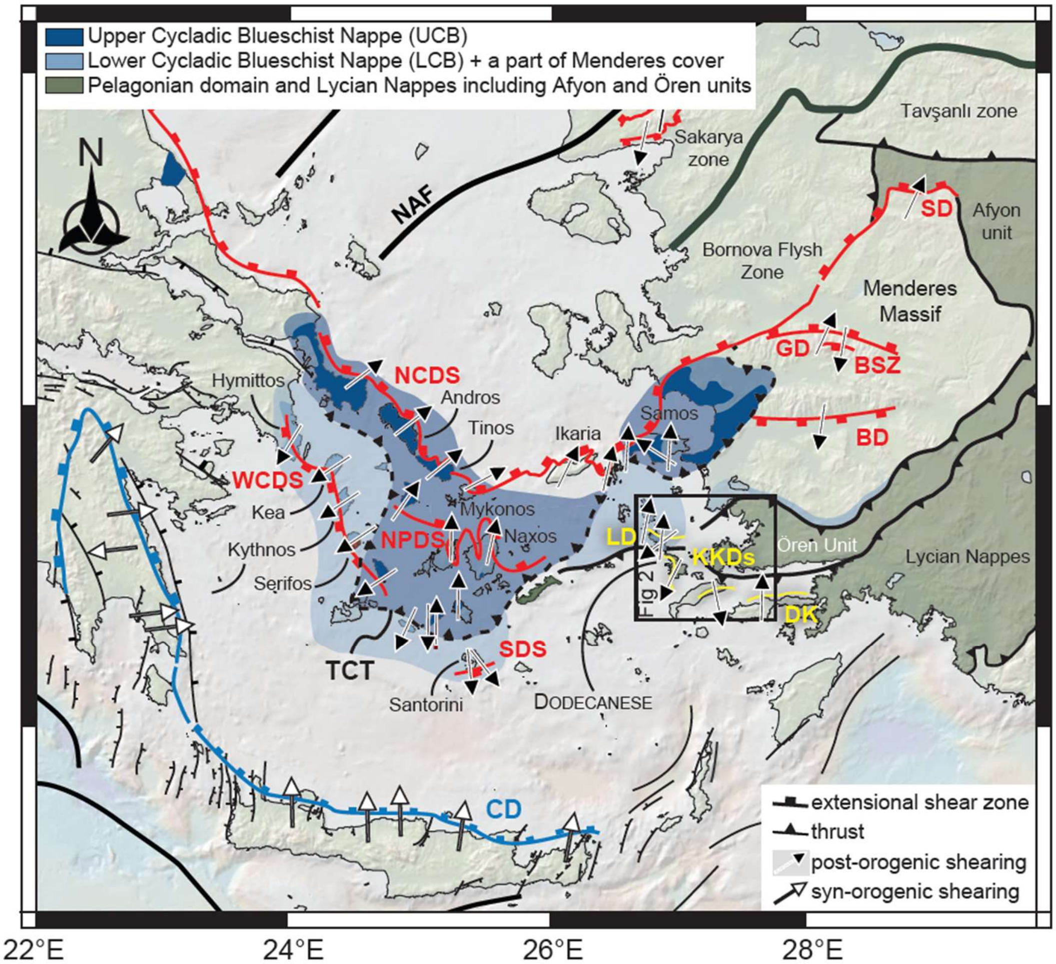

Figure 1: Tectonic map of the Aegean region modified after Roche et al. (2024). It shows kinematics of major Cenozoic faults during slab roll back. The blue and red lines correspond to syn- and post- orogenic extensional detachment; furthermore, the white and black arrows add the orogenic shear sense, respectively.

BD = Buyuk Menderes Detachment, CD = Cretan Detachment, DK = Datca–Kale fault, GD = Gediz Menderes Detachment, KKDS = Kalymnos-Kos Detachment System, LD = Leros Detachment, MSZ = Mouros Shear Zone, NAF = North Anatolian Fault, NCDS = North Cycladic Detachment System, NPDS = Naxos-Paros, Detachment System, SD = Simav Detachment, SDS = Santorini Detachment System, TCT = Trans-Cycladic Thrust, and WCDS = West Cycladic Detachment System.

2 Geological Setting

2.1. Aegean region

The geology of the Hellenides is subdivided into several different tectonic units from north to south with a focus on the south Aegean. The Vadar-Izmir Oceanic Unit or Vadar sutur zone consists of Jurassic ophiolitic rocks, which were subducted under the Srednogorie, Rhodope, and Sakarya continental fragments during the Cretaceous and was thrusted onto the Pelagonian unit. The Srednogorie, Rhodope, and Sakarya blocks represent the northernmost margin of the region, which is compounded with Eurasia. The Pelagonian Unit is composed of a Paleozoic Basement covered with Paleozoic and Mesozoic carbonate and topped by Jurassic ophiolite. The Pindos Unit is partly an oceanic-type sequence with late Triassic to Paleocene pelagic limestones and siliceous deposits covered by Eocene-Oligocene flysch and continental basement-cover sequences of the oceanic margin. On the Cyclades, the Cycladic Blueschist Unit (CBU) can be seen as a paleogeographic equivalent to the Pindos Unit. The Gavrovo-Tripolitza Unit is composed of a late Triassic thick marble sequence topped by late Eocene to early Oligocene metaflysch. In the south Aegean, the Gavrovo-Tripolitza Unit and the Pindos Unit are weakly metamorphosed. The Ionian Unit (or Plattenkalk) is composed of a base Mid-Liassic carbonate sequence, followed by a pelagic sequence until the late Eocene, and concludes with late Eocene to Miocene flysch. Together with the Gavrovo-Tripolitza Unit, the Ionian Unit was underthrust beneath the Pindos Unit in the Oligocene. The Pre-Apulian platform shows a continuous sequence until the Miocene with a transition to flysch (Jolivet & Brun, 2010, Ring et al., 2010). The Phyllite-Quartzite Unit consisting of continental to shallow marine siliciclastics and carbonates interlayered with vulcanoclastics of Triassic to late Carboniferous age, was exhumed beneath the Cretan Detachment during the Miocene (Jolivet & Brun, 2010 and references therein; Ring et al., 2010 and references therein).

The nappe complex of Kos is known for belonging to the external Hellenides (Bonneau, 1984; Franz et al., 2005; D. I. Papanikolaou, 2021; D. Papanikolaou & Nomikou, 1998; etc.). In recent works, the lithology of Kos was correlated with the Pelagonian Unit, which is predominantly exposed on several islands of the Dodecanese (Fig. 2). The Paleozoic Basement (i.e., Marina Basement Unit) and covered with upper Paleozoic limestone and wildflysch Unit (i.e., Kefala Unit) and/or a Mesozoic platform sequence (i.e., Marina Cover Unit). (Grasemann et al., 2022; Roche et al., 2024)

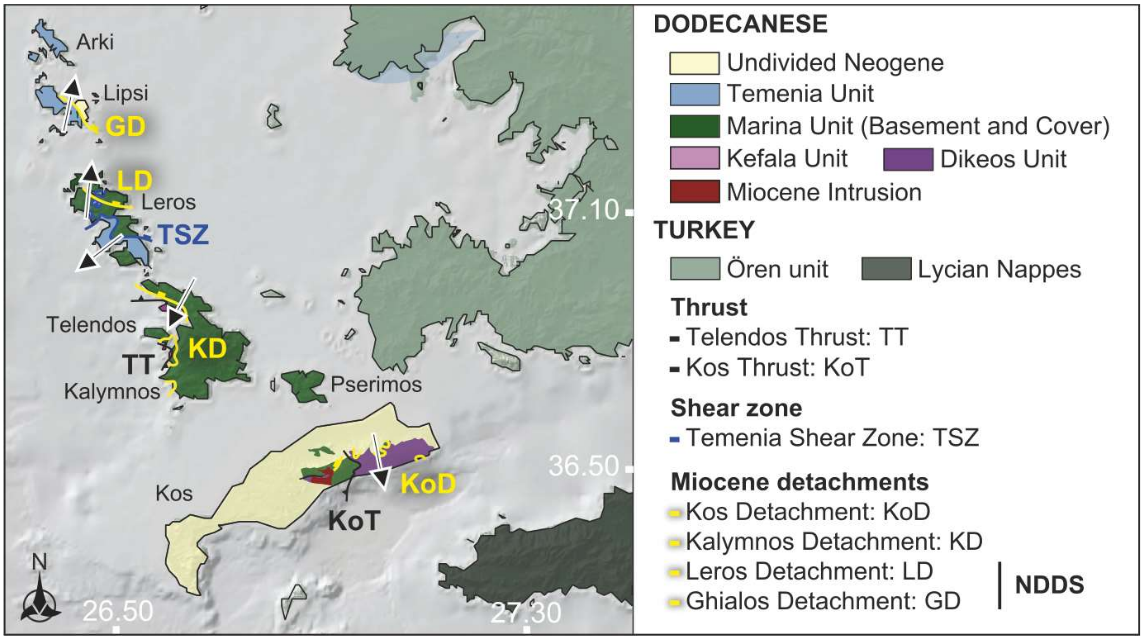

Figure 2: Tectonic and geological map of the Dodecanese islands Roche et al. (2024). Arrows indicate the post-orogenic shear sense.

2.2. Island Kos

Quaternary and Paleogene alluvial, marine, and volcaniclastic sediments cover almost three quarters of the island of Kos (Fig. 2&3a; further details e.g., Allen et al., 1999; Dürr & Jacobshagen, 1986; Willmann, 1983). The volcanoclastica were generated by the largest known eruption (161 ka) of the easternmost magmatic complex of the Aegean volcanic arc (Bachmann et al., 2019; Pe-Piper et al., 2005). During the L. Neogen, the active subduction zone of the Pliocene to Recent South Aegean Volcanic Arc (SAVA) and crustal extension in the Aegean create lamprophyre dykes penetrating the host rock of the island of Kos (Soder et al., 2016). Mesozoic Carbonates are exposed on the Kefalos peninsula and the Dikeos massif located in southeastern part of the island (D. Papanikolaou & Nomikou, 1998). The slopes of the mountain range of the Dikeos massif consist of Paleozoic rocks, corresponding to the Pelagonian Unit, which was penetrated by a large Miocene plutonic body (Altherr et al., 1976; Roche et al., 2024). The following tectonic subunits can be distinguished (Fig. 4):

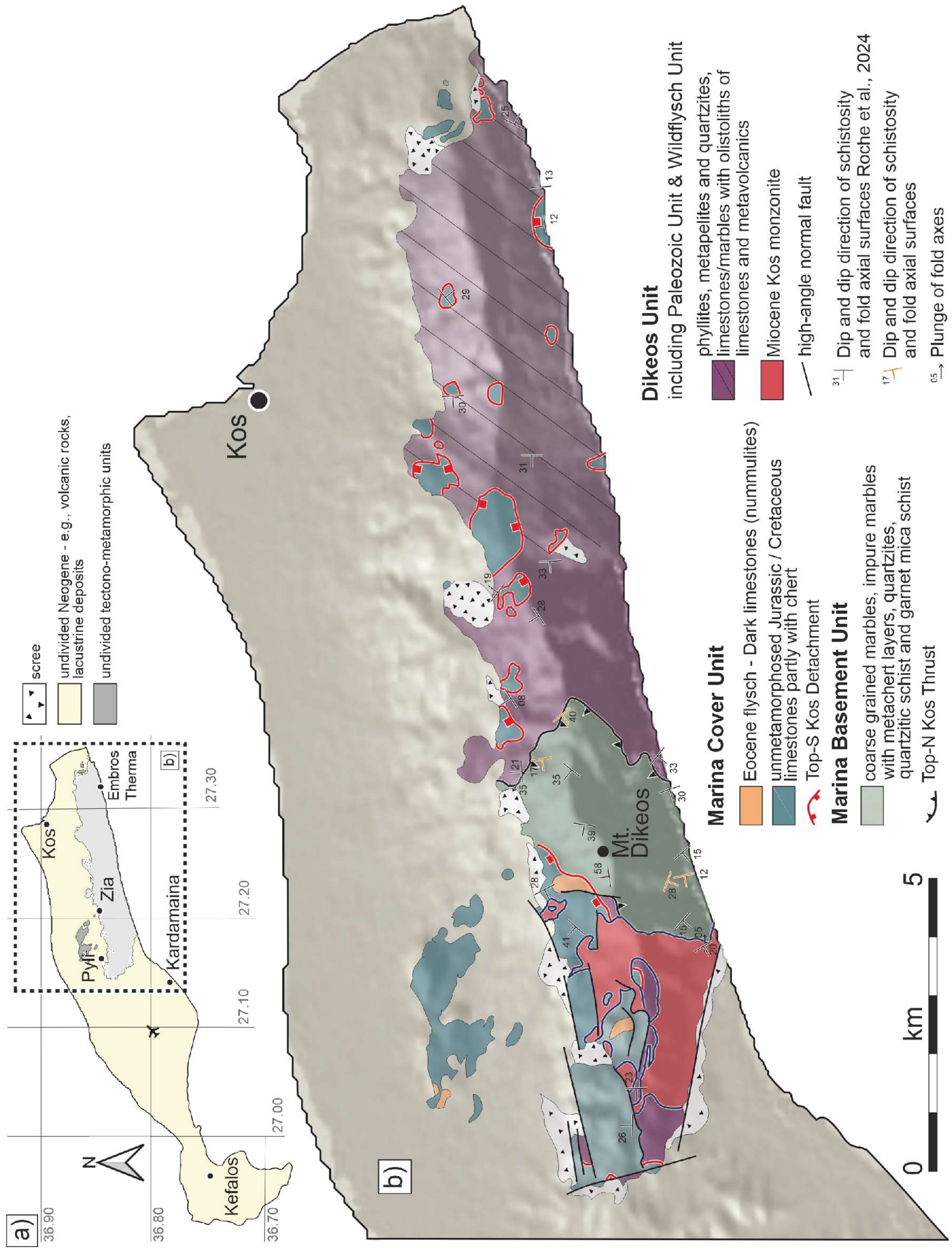

Figure 3: a) Simplified geological map of Kos b) Geological map of Kos, modified after Roche et al. 2024 with Dip symbols of this work and from Roche et al. (2024). The violet and cross-hatched area corresponds to the Wildflysch Unit.

2.2.1. Dikeos Unit (including the Paleozoic Unit and Wildflysch Unit)

The Dikeos Unit is exposed on the east of the Dikeos massif. It consists of a Paleozoic succession of meta-pelites, -sandstones, and -carbonates, which are divided by a tectonic contact separating the conformity of the Paleozoic (or Permo-Carboniferous Unit) and Wildflysch Unit (Dürr & Jacobshagen, 1986; D. Papanikolaou & Nomikou, 1998; Van Hinsbergen & Boekhout, 2009). Additionally, a Palaeogene age was set for the wildflysch (or Thermi flysch) because of the similarity to the Karabörtlen flysch in the Lycian Taurus (Altherr et al., 1982; Dürr & Jacobshagen, 1986).

However, the recent study of Roche et al., (2024) shows that the Dikeos unit is the lowermost tectonic unit on Kos, consisting of metapsammides to -pelites of lower greenschist facies and impure marble and meta-chert layers. Eastwards of the Paleozoic Unit, a gradational transition to the Permo-Triassic Wildflysch Unit with additional polymictic conglomerate layers and large olistoliths composed of metavolcanites, dolomitic limestones, and marbles in the form of large klippen (~300m diameter) occurs. However, the Dikeos Unit lacks tectonic contact between the subgroups (Paleozoic Unit and Wildflysch Unit). The metasediments generally dip towards the SW to NW, this derives from a large open dome structure. Although folds are rarely found in this unit, axial plane cleavages can be seen in most of the rocks. A metamorphic foliation slightly overprints the sediments without destroying the sedimentary bedding. There is no evidence of ductile high-strain deformation or ductile shear zones. (Roche et al., 2024)

2.2.2. Marina Basement Unit

The lithological content consists of coarse-grained pure marbles, impure marbles with metachert layers, quartzite- and schists. The metamorphic phases are primarily micas and garnets. The pure marbles consist of up to 3 mm polygonal calcite grains with sutured boundaries and deformation twins (Type II & Type IV). These rocks show a main foliation that changes its dip direction from steeply to the north on the northern slopes of Mt. Dikeos, to the west on the ridge, and towards the SW-SWW on the south slopes until the coastline (Fig. 3). The rocks endured polyphase ductile deformation causing Type 2 (mushroom) and Type 3 (hook and crescent) refold structures. Near the Kos Thrust the grain size of the marble is reduced, and the top-to-N shear sense becomes dominant. Near the intrusion on the mountain ridge and on the northern slopes of Mt. Dikeos partially highly sheared quartzites and mica schists host inter-tectonic garnet porphyroblasts that overgrow an earlier foliation. The garnet porphyroblasts have strain shadows and strain caps, with a mylonitic foliation wrapping around them. Some garnets show two different growth stages. (Roche et al., 2024)

At the western side, the Marina Basement Unit borders the Miocene monzonite body, which developed a contact aureole. The strong high-temperature metamorphic overprint forms skarn minerals such as andradite garnet and pyroxene, aa well as hornfels containing andalusite with fibrolithic sillimanite and cordierite. Mode I cracks cutting through all structures are filled with wollastonite. (Altherr et al., 1982; Roche et al., 2024)

2.2.3. Marina Cover Unit

The rocks of the Marina Cover Unit are Mesozoic non-metamorphic neritic carbonates (D. Papanikolaou & Nomikou, 1998), such as dolostones, dolomitic limestones and micritic limestones with thick chert layers (Roche et al., 2024). This unit was divided into various Units based on rock types, fossils, or paleogeographic analogues of the lithology (Altherr et al., 1976; Dürr & Jacobshagen, 1986; D. Papanikolaou & Nomikou, 1998). Particular is the former Zia Unit, which included the L. Eocene nummulitic limestones with flyschoid sediments terminating the succession (Blondeau et al., 1975). Although mostly covered by Upper Miocene to Pleistocene sedimentary rocks and volcanic tuffs, the Unit surrounds the Dikeos massif and is visible on the northern and south-eastern slopes of the mountain range. A reliable stratigraphic correlation of these Carbonates is impossible to define, since they are only preserved as klippen juxtaposed on the Dikeos Unit. The limestones have preserved bedding and sedimentary features. However, they are affected by dissolution-precipitation processes, indicated by stylolites. (Roche et al., 2024)

2.2.4. Monzonite Pluton

The intrusion body of Kos spreads over a surface diameter of 4 km and is located at the western end of the Dikeos massif (Triantaphyllis & Mavrides, 1998). There are two major intrusions mentioned, classified as monzonite and quartz biotite-hornblende monzonite, which are locally differentiated to monzogranite (for detailed information about the geochemistry see Altherr et al., 1976). Accumulations of large orthoclase crystals or bulks of elongated dioritic or monzodioritic mafic inclusions with a lack of alkali-feldspar, preserve a magmatic flow fabric. Most of the I-type pluton however is aphyric and contains a relatively high amount of biotite and hornblende. It was dated via biotite K-Ar, Rb-Sr, titanite fission track and (U-Th)/He (ZHe) dating to be 9-12 Ma old and record a moderately slow cooling. The monzonite of Kos was added to the list of Miocene I-Type, intrusions and a systematic regional variation of the composition based on the K_2O increase at constant SiO_2 was stated. The monzonite and the carbonates of the Marina Cover Unit are overprinted by roughly W-E striking high-angle normal faults (Fig. 3) with a top-to-N offset. Associated conjugated high -angle faults show a top-to-S offset, suggesting a brittle N-S extension. Along north-dipping high-angle normal faults in the higher structural levels of the granitoid, SC and SCC' fabric display a top-to-N shear sense (Altherr et al., 1976, 1982, 1988; Henjes-Kunst et al., 1988; Roche et al., 2024).

In the south-central Aegean Sea Miocene plutons comparable to the Kos intrusion body are widespread, especially in the Cyclades, with a close association to metamorphic core complexes of similar age (e.g. Bolhar et al., 2010; Henjes-Kunst et al., 1988; Kokkalas & Aydin, 2013; Stouraiti et al., 2010).

2.3. Deformation events on the island of Kos

2.3.1. Deformation of the Marina Basement Unit

The tectonic history of Kos starts with regional metamorphism of the Marina Basement Unit, creating Type 2 and Type 3 refold structures. The Paleozoic sediments were described to have experienced only anchimetamorphism (Altherr et al., 1976; D. I. Papanikolaou, 2021; Van Hinsbergen & Boekhout, 2009).

2.3.2. Kos Thrust

A tectonic contact on the northern slopes near the hiking trail to the top of Mt. Dikeos was first described by D. Papanikolaou & Nomikou, (1998). A thrust that juxtaposes the former Tripolis Unit (now Marina Cover Unit) over the eastern Kos wildflysch (now Dikeos Unit) was, according to Roche et al. (2024), replaced by a top-to-N Eocene thrust. It crops out east of the peak, pushing the Marina Basement Unit on the Dikeos Unit. A Change from white coarse-grained pure calcite marble to rather impure marble mylonites is realized by an increasing strain gradient toward the thrust plane, where fabrics of the low grade Dikeos Unit and the higher-grade metamorphosed Marina Basement Unit are overprinted by top-to-N kinematic indicators, mainly dominant SC and SCC' fabrics. Additionally, the thrust zone bends over the mountain range of the massif; that is why the dip angle changes from 25-30 ° toward top-to-N, to a top-to-W, and finally to a top-to-SW on the southern slopes of Mt. Dikeos. The fault rock consists of cataclasites with truncated clasts of a quartzofeldspathic protolith. (Roche et al., 2024)

2.3.3. Kos Detachment

Initially, a thrust between the Paleozoic Unit and the Wildflysch Unit was described (Papanikolaou and Nomikou, 1998); however, this tectonic contact was later revised to be a late Miocene top-to-N Kos Detachment (Van Hinsbergen & Boekhout, 2009). The paper of Roche et al. (2024) suggested that the contact is rather a gradational depositional horizon than a tectonic one (Fig. 3b).

The Kos Detachment spreads over the whole Dikeos massif and runs at the Base of the Marina Cover Unit with its carboniferous klippen (Triantaphyllis & Mavrides, 1998). The footwall is represented by the Paleozoic metasediments belonging to the Marina Basement Unit and the seds and wildflysch belonging to the Dikeos unit. Due to a dome shape of the modern detachment planes, the dip directions are not uniform and show a variation, but in general, a NNW-SSE trending stretching lineation with a top-to-SSE shear sense can be ascertained (Fig. 5b). At the fault surface a thick fault clay gouge, contain the striations and SC, SCC' fabrics, crushed sigmoids and winged inclusions were used as kinematic indicators. Through the movement of the detachment, north dipping high-angle normal faults are generated. The Kos Detachment can be correlated to the Kalymnos detachment, which has 30 Ma weighted mean ZHe ages. (Grasemann et al., 2022; Roche et al., 2024)

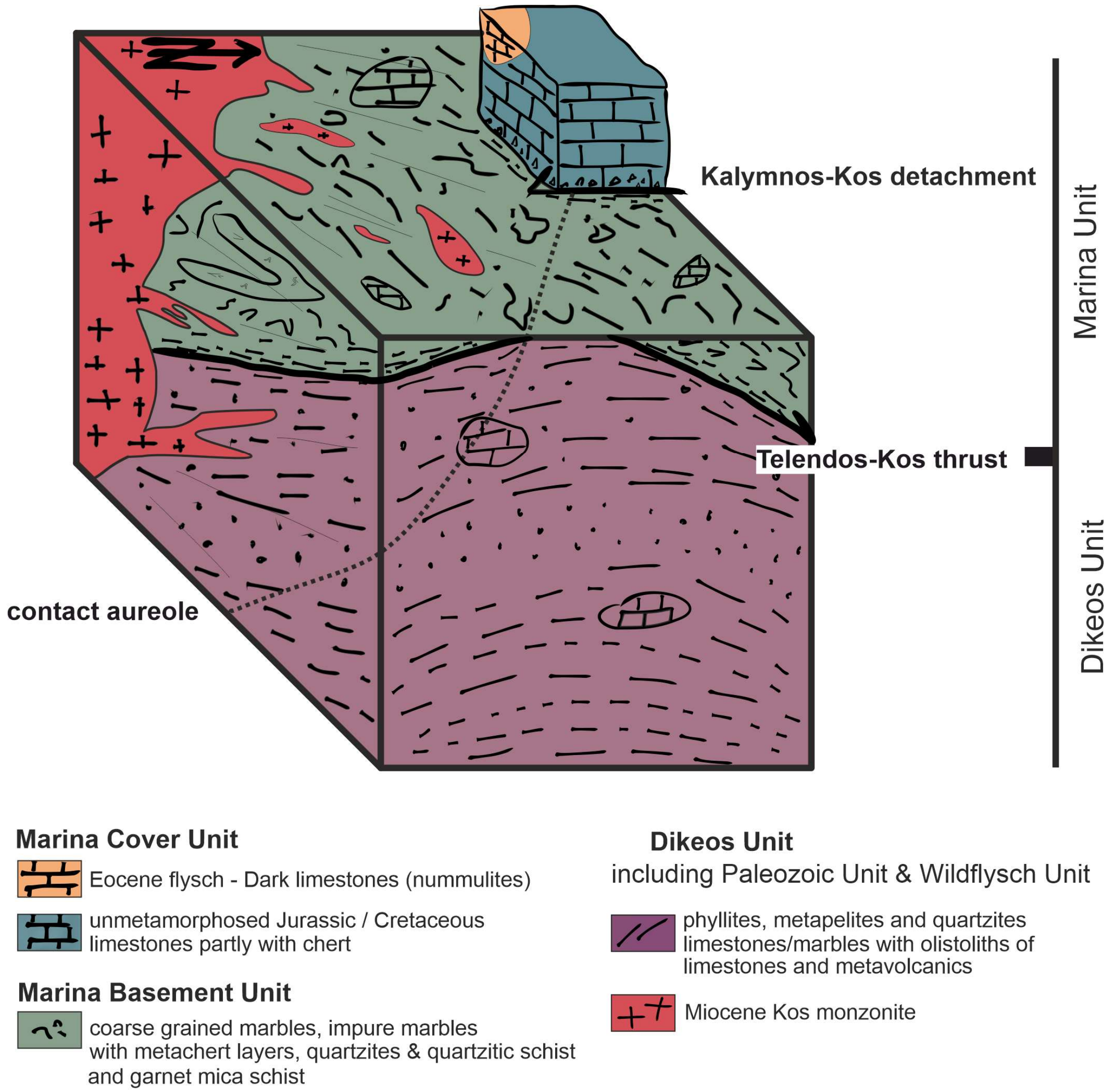

Figure 4: Synoptical 3D-diagram summarizing field, microstructural observations, and measurements of Roche et al. (2024) of Kos (not to scale). It roughly displays the lithologic units, main tectonic contacts with their respective kinematics, and the influence of the monzonitic intrusion.

3 Methods

3.1. Fieldwork & Sampling

The fieldwork was conducted to obtain a broad range of samples and to gain an on-site overview of the geological setting of the Marina Basement Unit, also referred to as the Paleozoic basement. Consequently, all lithological variations within the unit, as well as the contact zone of the intrusion, were considered relevant for this study. The Marina Basement Unit constituted the primary research area, as illustrated in the modified map (Fig. 5), adapted from Roche et al. (2024). The study by Kalt et al. (1998) served as a reference for selecting sampling locations. However, additional specimens were collected from outcrops, particularly in proximity to and beyond the intrusion. All coordinates are provided in the WGS 1984 Universal Transverse Mercator (UTM) Zone 35S coordinate system. The legend includes all sample points used for microstructural and petrological analyses. Furthermore, the outcrop locations of the chronological specimens from Roche et al. (2024) are indicated. For improved clarity, structural measurements are shown in Fig. 3 and thermometric data are presented in Fig. 29. In this study, particular emphasis was placed on the range of metamorphic overprints observed in the collected samples. Accordingly, a loose piece of an Endoskarn found within alluvial deposits was included for comparative purposes. In addition to lithological characteristics, structural geological aspects were also taken into account.

Following the fieldwork, all specimens were re-evaluated. Samples exhibiting significant alteration, redundancy, or those deemed unnecessary for the scope of the study were excluded to reduce the overall sample volume. The remaining specimens were cut perpendicular to the foliation and parallel to the stretching lineation, corresponding to the XZ-plane of the finite strain ellipsoid. Thin section preparation for optical microscopy, scanning electron microscopy (SEM), and electron microprobe analysis (EPMA) was carried out at the thin section laboratory of the Faculty of Earth Sciences, Geography and Astronomy, University of Vienna. Thin sections for optical microscopy were prepared with a thickness of 30 microns, polished, and covered with a glass plate to ensure a smooth surface and clear visibility of the mineral assemblage, while also preventing contamination. This facilitated the identification of mineral phases and microstructures. Sections for EPMA were prepared at a thickness of 50 microns, and those for SEM at 30 microns, as slices must exceed 30 microns in thickness. After polishing, a carbon coating was applied to prevent charging effects on the surface (Reed, 2005). These sections were not used for petrographic analysis, so incorrect interference colors were not a concern. An additional advantage is that the sections remain re-polishable for future use.

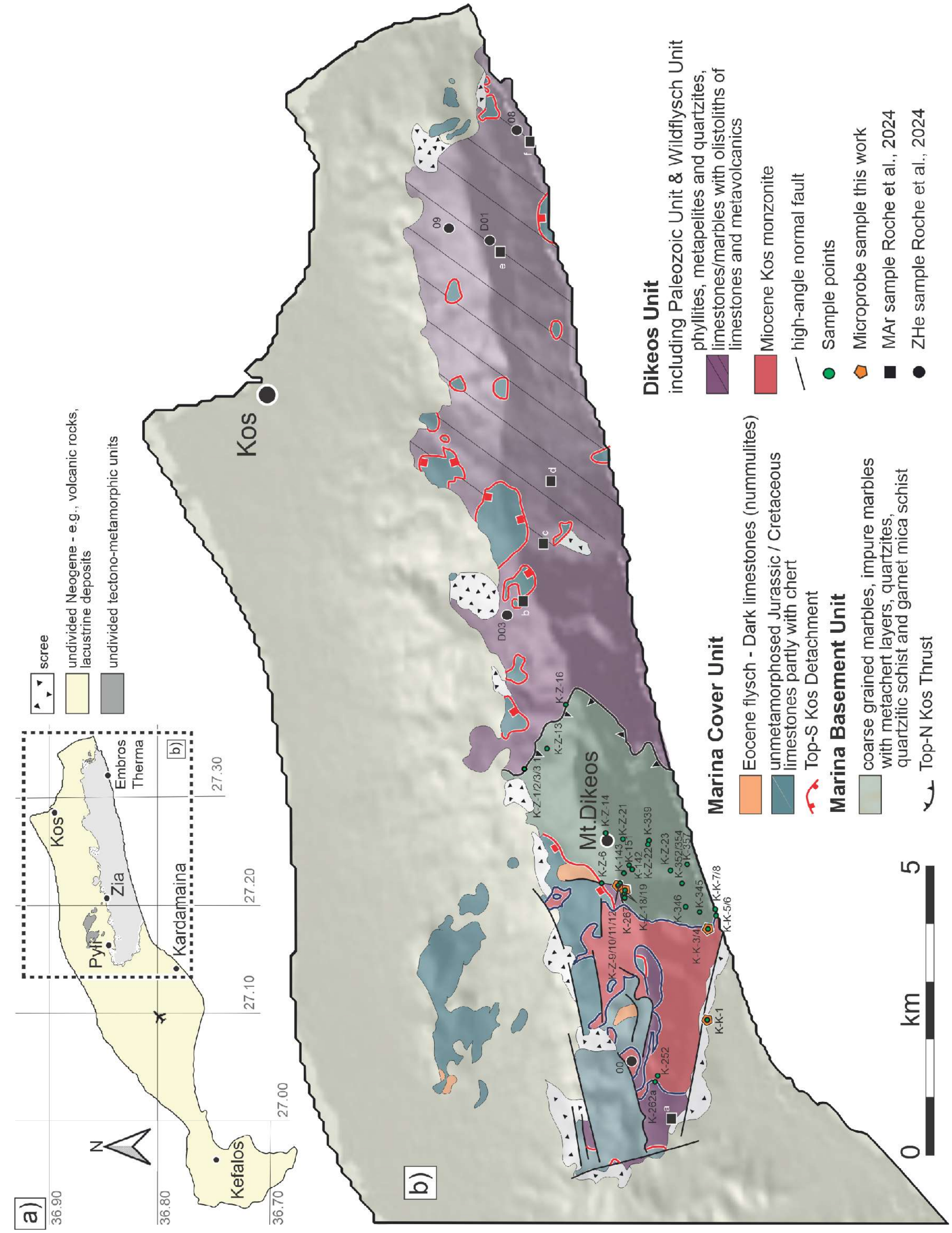

Figure 5: a) Simplified geological map of Kos b) Geological map of Kos, modified after Roche et al. (2024) with the sample locations of this work and of the geochronological samples of Roche et al. (2024).

3.2. Microstructural & Petrographic analysis

For petrographic and microstructural investigations, the optical polarized light microscope Nikon Optiphot-2 was used. The images presented in this study were captured using a Leica DM4500 P LED equipped with a Canon EOS R6 Camera. For stitched images, a Leica DM4500 P with a motorized microscope stage (XY-control) was used. Pictures of a hole thin section were produced by a Nikon Super Coolscan 5000 Diascanner.

3.2.1. Scanning electron microscope (SEM)

The SEM analyses were conducted using a TESCAN VEGA 4 (Faculty of Earth Sciences, Geography and Astronomy, University of Vienna), equipped with a tungsten hairpin filament. This instrument was used to acquire secondary electron (SE) images, back-scattered electron (BSE) images, cathodoluminescence (CL) images, and energy-dispersive X-ray spectroscopy (EDX) data.

Carbon coating was applied using a Safematic CCU-010 system, which deposited a fine 4 nm layer of carbon under vacuum conditions ($\sim 7 \times 10^{-5}$ mbar). This coating minimizes the loss of primary electrons while maintaining compatibility with optical microscopy. After coating, the specimens were mounted on aluminum sample holders using silver suspension, which was applied both on the mount and along the edges of the thin sections to ensure stable electron flow to the SEM grounding.

3.2.2. Electron probe micro analysis

Major element compositions of selected mineral phases were determined using a CAMECA SXFive FE electron microprobe (Faculty of Earth Sciences, Geography and Astronomy, University of Vienna). Carbon coating for EPMA was provided by the thin section laboratory (Faculty of Earth Sciences, Geography and Astronomy, University of Vienna).

The EPMA is equipped with five wavelength-dispersive spectrometers (WDS) and one energy-dispersive X-ray spectrometer (EDX). Routine point analyses were performed on garnet and ilmenite under the following conditions: 15 kV accelerating voltage, 20 nA beam current, 20 s counting time on peak position, and a spot size of 1 µm. For some garnet porphyroblasts, profile lines were measured with an approximate spacing of 20 µm between points. For biotite, the electron beam was defocused to 5–7 µm, and the counting time on peak position was reduced to 10 s. Calibration of the microprobe was carried out by the instrument operator, and a ZAF correction was applied. Some garnet measurements slightly exceeded the relative precision threshold of ±1 rel.% (2σ) (Reed, 2005); these data points were excluded from normalization calculations.

3.2.2.1. Normalization

To determine the endmember compositions of the investigated minerals, quantitative data from electron microprobe analyser (EPMA), given in weight percent of cation oxides (e.g., SiO_2, CaO), must be normalized. For garnet, the general formula $X_3Y_2Z_3O_{12}$ requires eight cations and 24 charges. The X-site is typically occupied by divalent and monovalent cations (Ca^{2+}, Fe^{2+}, Mg^{2+}, Mn^{2+}, Na^{+}), the Y-site by trivalent cations (Al^{3+} & Fe^{3+}) and the Z-site by Si^{4+} and Al^{3+}. The Y-site often exhibited vacancies, which were filled by bivalent cations (Fe^{2+}) and tetravalent cations (Si^{4+} & Ti^{4+}). Ideally, the Z-site is fully occupied by Si^{4+}. However, due to site deficiencies and charge balance considerations, Al^{3+} may substitute into the Z-site. Similar substitutions can occur for the Y-sites. The X-site and Y-site composition determines the garnet species, based on the given divalent and trivalent cations. Iron requires special consideration, as both Fe^{2+} and Fe^{3+} must be distinguished to ensure charge balance and a fully occupied crystal lattice, which are assumed for endmember determination. For biotite, precise normalization is limited due to the presence of volatile components such as OH^{-} and F^{-}, of which OH^{-} cannot be measured directly by EMPA. Consequently, distinguishing between iron oxidation states is not possible in this context, because deviations of the oxide sum from 100% could be due to either the presence of OH^{-} or Fe^{x} oxidation state variations.

3.3. Raman Spectroscopy of Carbonaceous Materials (RSCM)

The preparation and acquisition work followed the analytical procedure outlined by Rantitsch & Linner (2021). All samples were checked for substantial carbonaceous material (CM) content, and 10 specimens were selected (see results). Small pieces of the chosen samples were detached and manually crushed with a hammer to obtain coarse fragments (mm). Before treatment with hydrochloric acid (HCl ~36%) and hydrofluoric acid (HF 40%) in separate runs, the material was ground in an agate mortar mill and then sieved (<125 µm) to achieve a relatively homogeneous powder. The acidified samples were placed in cylindrical Teflon containers and heated on a hot plate for about one hour to enhance the dissolution process. After each acid treatment, a centrifuge was used to separate the powder and decant the supernatant. The residue was slurred with distilled water to remove any remaining acid and centrifuged again. This workflow was repeated three times to achieve satisfactory results. To ensure a uniform distribution of particles, the dried powder was mounted as a water suspension on glass sample plates. After the suspension had dried, no further manipulation, such as polishing, which could alter the CM, was applied. (for further information see: Lünsdorf (2016); Rantitsch & Linner (2021))

The Labram HR Evolution instrument at the Chair of Resource Mineralogy of the Technical University of Leoben was used to acquire Raman spectra. The device was equipped with a 100 mW Nd-YAG laser (532 nm), a diffraction grating of 1800 g/mm, and a Peltier-cooled CCD detector. An Olympus BX-FM open microscope with a 100x objective lens (0.80 numerical aperture (NA)) was used for the optical setup. For confocal measurements, the hole aperture was set to 100 µm. The laser output power was set to <1 mW to avoid burning organic matter. The wavenumbers were calibrated using Rayleigh scattering (0 cm−1) and a silicon wafer (520.7 cm−1). Each spectrum was acquired with a 20-second acquisition time and two accumulations to improve the signal-to-noise ratio. (Rantitsch et al., 2020; Rantitsch, 2024)

All spectra were processed using the IFORS software following Lünsdorf & Lünsdorf (2016) for the first order (700-2000 cm-1) and second order (2200-3200 cm-1), which was modified after Rantitsch (2023). RCSM data was calibrated after Lünsdorf et al. (2017) for the first- and Rantitsch (2023) for the second-order Raman spectra. The software allows iterative and random-based curve-fitting without direct user interaction, significantly reducing spectral processing bias (Fig. 6); (Lünsdorf et al., 2017; Rantitsch & Linner, 2021). These spectral regions contain the important CM bands for determining the metamorphic peak temperature during regional and contact metamorphism (Henry et al., 2019; Nemanich & Solin, 1979; Tuinstra & Koenig, 1970). Note that the RSCM reference data used only regional metamorphic samples; thus, a significant influence of the contact metamorphism cannot be ruled out.

In the first order, two main band regions are important. The graphite band at ~1580 cm^{-1} (G) is generated by the vibration mode of the ideal in-plane graphite lattice, and the main D-band at ~1340-1360 cm^{-1} (D1-band) occurs due to a disordered graphitic structure from structural defects or heteroatoms. The second order is represented by the main S-band at ~2700 cm-1 (S2-band), which splits into two individual bands when the CM is highly ordered and is actually the 2D-band, an overtone of the D1-band. Up to six D-bands and four S-bands can arise. The distance of the new S-bands increases as a response to rising temperatures. The provided nomenclature for CM bands is based on (Henry et al., 2019). (Henry et al., 2019; Rantitsch, 2023; Rantitsch & Linner, 2021)

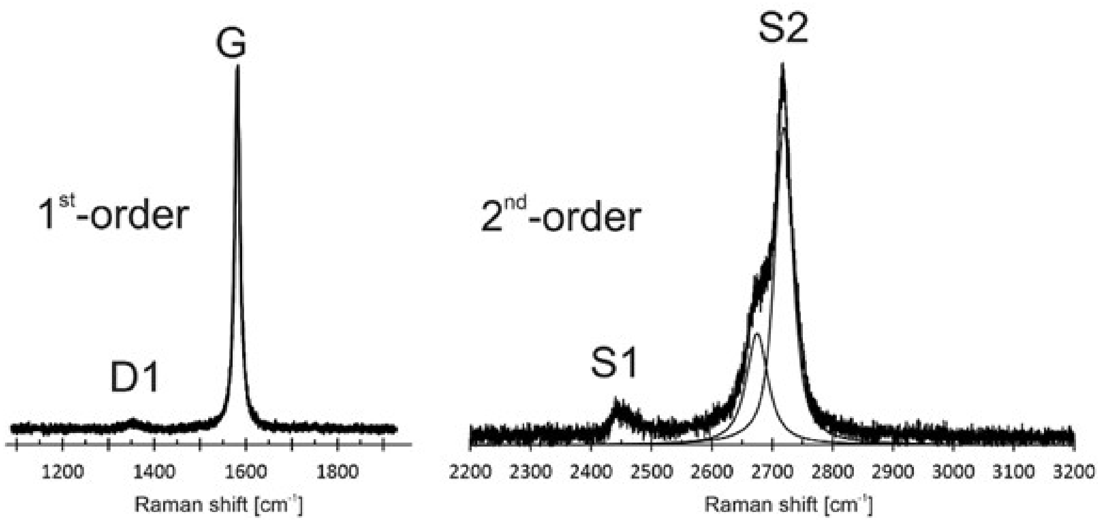

Figure 6: Representative 1st- and 2nd-order Raman spectra of graphite (from Rantitsch & Linner et al., 2021) in the 600 °C region showing a sharp G-band, a D1-band of very low intensity, and asymmetric S1 and S2-bands. A potential D2-band at the right shoulder of the G-band is not visible. The S2-band is split into two Pseudo-Voigt functions. The 2nd order spectra gain importance for undisturbed or highly ordered graphitic lattices at higher temperatures (Sadezky et al., 2005). (Rantitsch & Linner, 2021)

According to Lünsdorf et al. (2017), the median of all collected first-order spectra was used to characterize the spectral parameters. The G-shape factor determines which STA (Scaled Total Area) value should be used. The Gmax_position, Dmax_position, and notably the G_STA parameter, which provides the sum of all intensity values of all implemented pseudo-Voigt functions of the curve-fitted spectrum scaled to the G maximum intensity, were considered. (Lünsdorf et al., 2017; Lünsdorf & Lünsdorf, 2016; Rantitsch & Linner, 2021) The evaluated results from the IFORS software were provided by Professor Dr. Gerd Rantitsch from the Technical University of Leoben.

4 Results

4.1. Structural analysis of the Marina Basement Unit

4.1.1. Field, Microstructural & Petrographic observations

The Marina Basement Unit consists of coarse-grained pure marbles, impure layered marbles with metachert layers (Fig. 11), quartzite- and mica schists (e.g Fig. 9b), occasionally with garnet or chiastolite porphyroblasts (Fig. 8b). The Marina Basement Unit is, at all scales, a lithologically inhomogeneous Unit, whereas the purer marbles build up klippen that dominate at the mountain ridges of the Dikeos massif (Fig. 7a).

Figure 7: (a) The Marina Basement Unit with marbles in front and klippen on the top of the mountain range. The valley opening towards the south exposes the lithologically inhomogeneous nature of the Unit, which is composed of alternating marbles and quartzitic schists. (b) The Dikeos mountain range heading west with the Marina Cover Unit on the northern slopes and the monzonite on the southern slopes; Kefalos peninsula in the back (KZ-18; 517541E, 4076116N). (c) The geological contact between the Marina Basement Unit and the Kos monzonite (KK-3 &KK-4; 526952E, 4074386N); (d) Monzonite with a magmatic flow fabric of the melanosome enclaves (515380E, 4074487N).

The monzonite intrusion pierces the Paleozoic Units in the west, south of the Marina Cover Unit (Fig. 7b). The plutonic rocks show typical spheroidal weathering, resulting in rounded blocks, which often remain embedded in a matrix of weathered material (saprolite), and can eventually become exposed due to erosion, forming striking landscapes with isolated, rounded monzonite boulders. Most of them have mafic dioritic enclaves and elongated alkali feldspars, oriented by magmatic flow (Fig. 7d; Roche et al., 2024). For further information on the monzonite see e.g. Altherr et al. (1976, 1982, 1988). At the contact of the intrusion (Fig. 7c), the metasediments get overprinted by high-temperature contact metamorphism. Hornfels rocks (Fig. 8a&b) host skarn minerals such as andalusite (some in the variety of chiastolite), cordierite, garnet, scapolite, sillimanite (in the variety of fibrolites; Fig. 8c&d; Vernon, 2018), pyroxene, and wollastonite which were generated. Despite the dominant thermal overprint and the formation of a poikiloplastic mineral structure in a hornfels, a sharp and clear foliation is conserved. Prismatic andalusite is unstable, breaking down into symplectites and tabular biotites, which are randomly oriented (Fig. 8d). The chiastolite has elongated prisms with a square to rhombic shaped cross section and an altered sericite rim, within a fine-grained matrix rich in biotite, muscovite and graphite (Fig. 8a). In thin section K-339, a vertical fault zone crushes and highly alters the chiastolite porphyroblasts and the surrounding matrix.

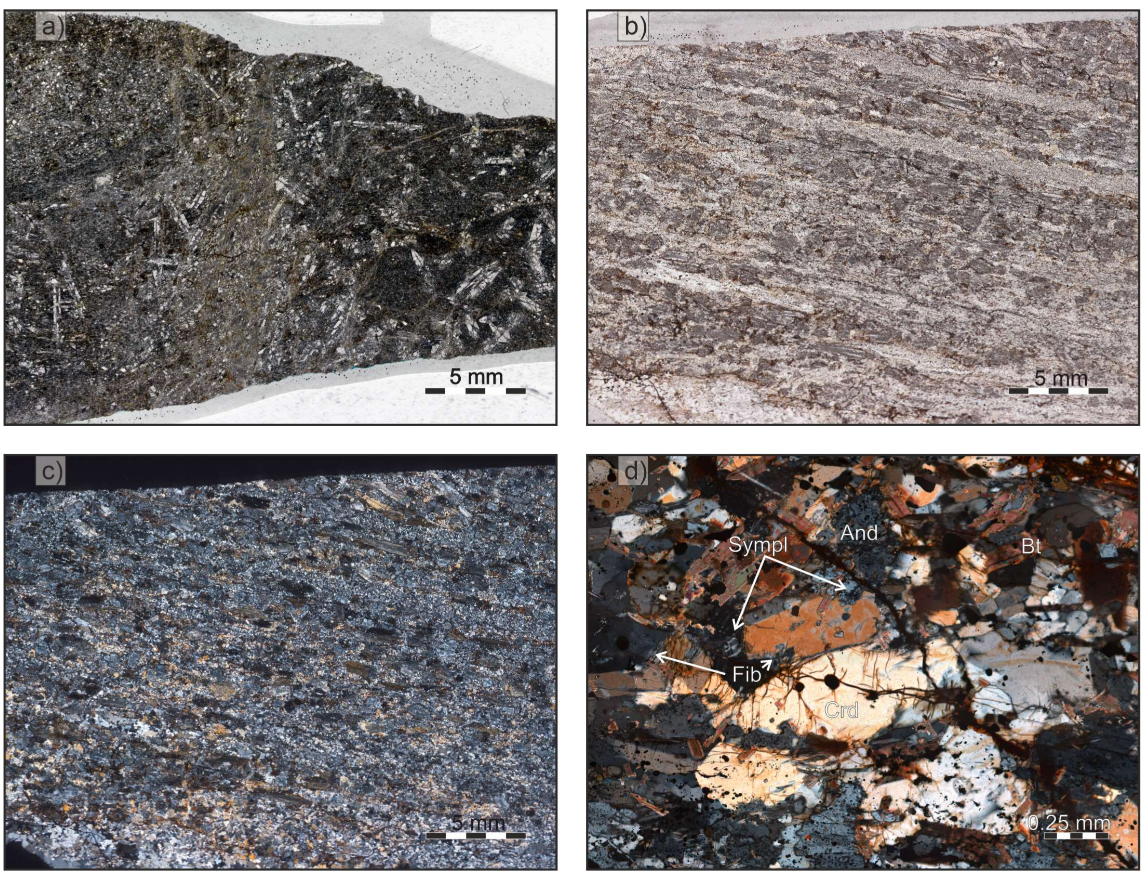

Figure 8: Thin section scans and photomosaics display the high temperature overprinted rocks. (a) Thin section scan (XPL) of a graphite-rich andalusite-mica schist or graphite-rich andalusite-nodular shale. The andalusite occurs as chiastolite in the form of mm-long elongate prisms. (K-339; c, 518473E, 4075804N) (b) Thin section scan (PPL) represents a hornfels picked close to the monzonitic intrusion. A sub-horizontal foliation runs over the hole section. (c) Same thin section scan (XPL), where contact metamorphic minerals like the elongated prismatic chiastolite can be differentiated from the plagioclase and quartz layer. (d) Photomosaic (XPL) of the paragenesis cordierite, and polygonal andalusite together with sillimanite. (K-262a; d, e, f; 514230E, 4075172N)

The skarns follow or crosscut the pre-existing foliation. In proximity to the coastline and the contact with the monzonite, a quartzitic mylonite shows grains with undulous extinction and SGR (Fig. 9a). The mylonite is cut by mode I cracks. Along the foliation, a fissure is filled with wollastonite. Clinopyroxenes (hedenbergite, diopside) has symplectitic structure with plagioclase and create a rim around the radially grown wollastonite crystals, which themselves get rimmed by garnet (Fig. 9a-i).

The quartzitic mylonite shows a strong foliation of opaque layers of fine-grained graphitic quartz and biotite. Isoclinal folding with fold axes parallel to the stretching lineation indicate high-strain. Monoclinic structures like sigmoids indicate top to SSW shear sense. The strong contact-metamorphic overprint is confined to c. 300-500m to the intrusion. Outside the contact-metamorphic aureole hornfels with chiastolite and mica schists with up to 3mm large garnet porphyroblasts were found. Chiastolite relicts appear as altered skeletal porphyroblasts flowing in a mica graphite matrix of a quartz-rich mica schist. These mineral associations can be found even >2km away from the mapped intrusive contact, e.g. at sample location K-Z-3. Apart from the calc-silicate, most of the Marina Basement Unit shows pressure-dominated rather than temperature-dominated structures. The metamorphic phases of the schists mainly consist of quartz, Na-rich plagioclase, and biotite. In some samples, amphibole, chlorite, and rarely white mica occur. Ilmenite is a very common phase in all schists and occasionally forms larger aggregates. Hercynite and rutile are further accessory ore minerals.

All these rocks show a main foliation that changes its dip direction from steeply to the north on the northern slopes of Mt. Dikeos, to the west on the ridge, and towards the SW-SWW on the south slopes and the S coast (Fig. 3). In the quartzitic mica schists, pinch and swell structures record foliation parallel to the stretching. Brittle/ductile shear bands offset the foliation, indicating a component of shear deformation (Fig. 9 b). In the thin section, a quartzitic layer shows a pinch and swell structure that itself is deformed by a SCC' structure (Fig. 9c). A calcite pinch-and-swell structure is observed, with the neck composed of amphibolite and scapolite. An isoclinal fold is present between scapolite and quartz grains, highlighted by a bold white line (Fig. 9d). A SSC' fabric offsets the foliation and records a top-to-E shear sense (Fig. 9e). Quartz veins cut the hole fabric normal to the foliation.

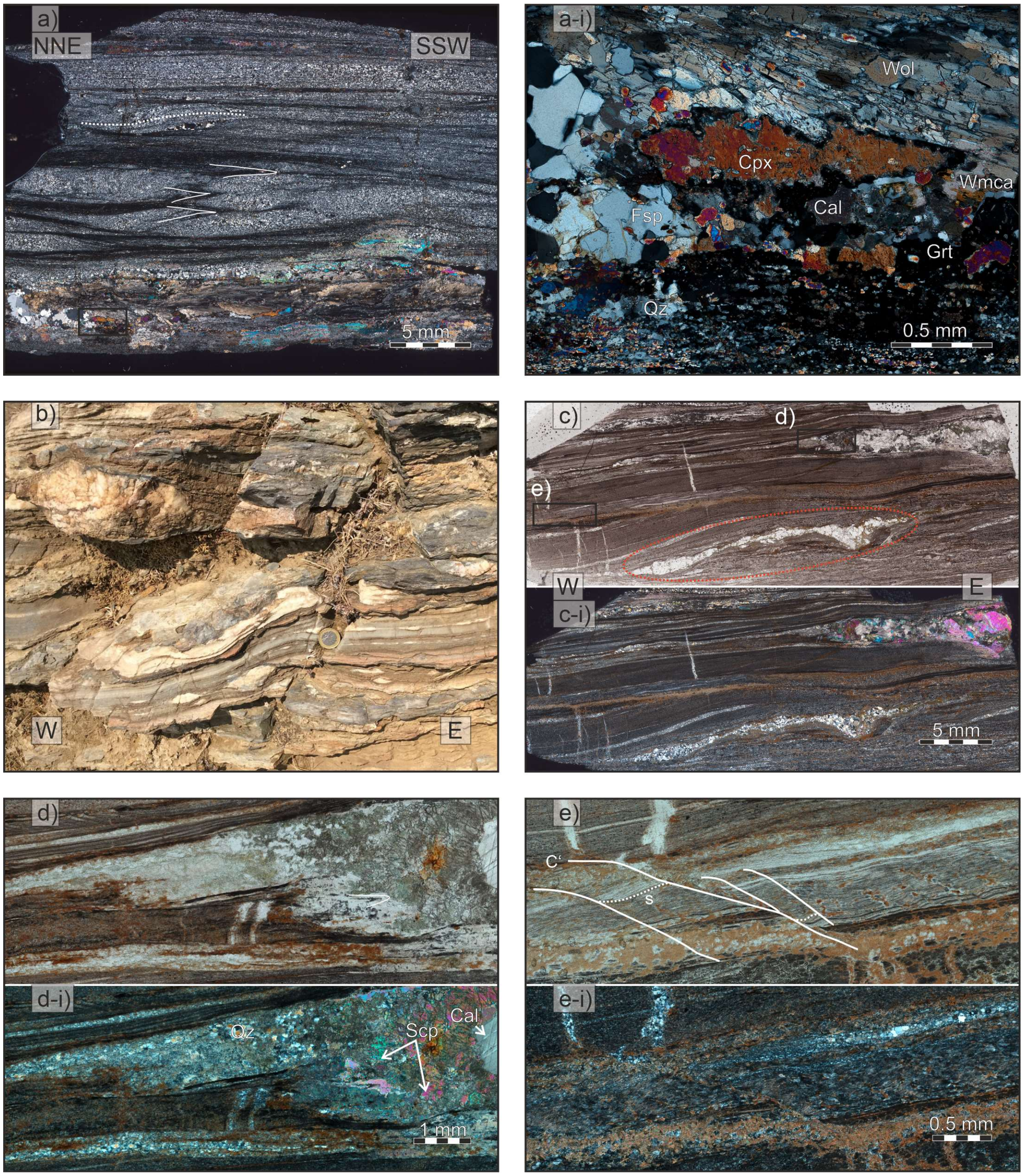

Figure 9: Illustrations of typical layered metasediments of the Marina Basement Unit, which are skarn related. (a) Thin section scan (XPL) of a foliated quartzitic schist with isoclinal folds accentuated by white solid lines and a possible sigmoid with a black dotted median line and a Top-to-S shear sense; At the bottom, a skarn intrusion (wollastonite) interrupts the layering. A rim of clinopyroxene surrounds the wollastonite band. (a-i) Photomosaic of clinopyroxene that has a garnet rim adjacent to a wollastonite rim. (KK-8; a; 517353E, 4074360N) (b) A mylonite with calcite and quartz pinch and swell structures is cut by subvertical joints. On the right side of the coin, the sample K-357 was taken. (c) Thin section scan (PPL) depicts a calcite swell and a quartzitic pinch and swell structure marked by a red dashed ellipse. Photomosaics (d) and (e) are localized by black squares. (e) Photomosaic in the neck of the calcite swell are scapolite grains (Scp) and an isoclinal fold hinge highlighted by a solid white line. (f) Photomosaic of a SCC' fabric cuts throw thin layers of the phyllonitic matrix indicating a Top-to-E shear sense. (K-357; b, c, d, e; 518136E, 4075078N) The thin section images c, d, e do have their cross polarized (XPL) counterpart below (X-i).

The entire unit shows Type 2 (mushroom) and Type 3 (hook and crescent) refold structures (Fig. 10a) with isoclinal folds (f1) incorporated in the limbs of the folds (f2) (Fig. 10b). The intrafolial isoclinal fold generation (f1) has acute fold hinges and are difficult to spot in the outcrop but frequently observed in cut and polished hand samples and in thin sections (Fig. 10b,c&d). The impure marbles close to the Kos Thrust even depict a cylindrical fold (f2) with a fold axis trending to the E. The recumbent fold reveals folded isoclinal folds (f1) in its upper limb creating a type 3 interference pattern (Fig. 10e).

Near the Kos Thrust, the grain size of the marble is reduced and the top-to-N shear sense becomes dominant (Fig. 11a). A SSC' structures (Fig. 11b) and sigmoids (Fig. 11c) indicate top-to-N shear sense. In the thin section, pure calcite layers with deformation lamellae and twins alternate with calcite laminar containing fine graphitic or mica impurities (Fig. 11d). The marble hosts a lot of ataxial grown calcite veins. A sigmoid with calcite deformation twins is next to a calcite vein, displaying an asymmetric shear band boudinage (Fig. 11d-i). An impure calcite layer is cut by calcite veins, creating another asymmetric shear band boudinage, which seems to be rotated (Fig. 11d-ii) as well as a shear band (Fig. 11d-iii). All structures indicate a Top-to-NW shear sense.

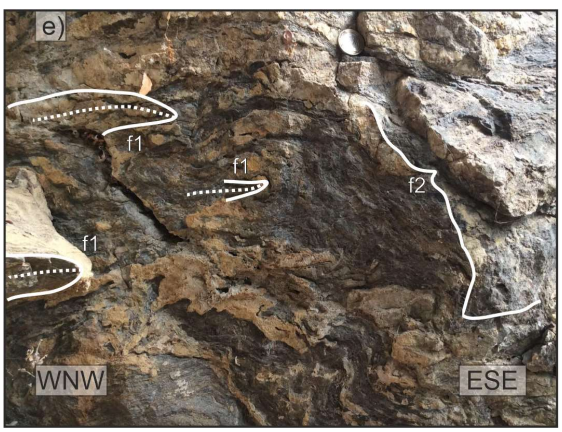

Figure 10: Images and a thin section scan of the folded metasedimentary Marina Basement Unit. (a) The impure and quartz-rich schists layered marble record a Type 2 and Type 3 interference pattern. Within tens of meters to the left of the picture the monzonite intrusion cuts the refolded marble - modified image from Roche et al., 2024 (516921E, 4074517N); (b) A block made of impure marble with interlayered quartz-rich schists. The hole block seems like a fold core, but it depicts a clear hook of a Type 2+3 refolds structure. Internally, there is a complex pattern of higher-order folds. However, close to the fold hinges are more dominant folds representing the two different fold generations f1 + f2. (514213E, 4075112N); (c) The collected loose hand sample of quartz-rich mica schists is highlighting the Type 2 and Type 3 refold structure. (KZ-22; 518402E, 4075813N); (d) Thin section scan (PPL) of a fold hinge from the specimen (KZ-22/(c)). The schist is predominantly composed of fine grains (~25 microns). The two different fold generations are well defined by carbonaceous material and micas, where a f2-fold overprints the older fold event f1. (e) An impure layered and refolded dark marble with remains of pure calcite veins on the surface (see Fig. XX) (KZ-13; 519848E, 4077807N). The solid white line marks the trace of the refolded metamorphic layering. The dotted white line follows the trace of the axial surface of the first (f1)- and second fold (f2) generation.

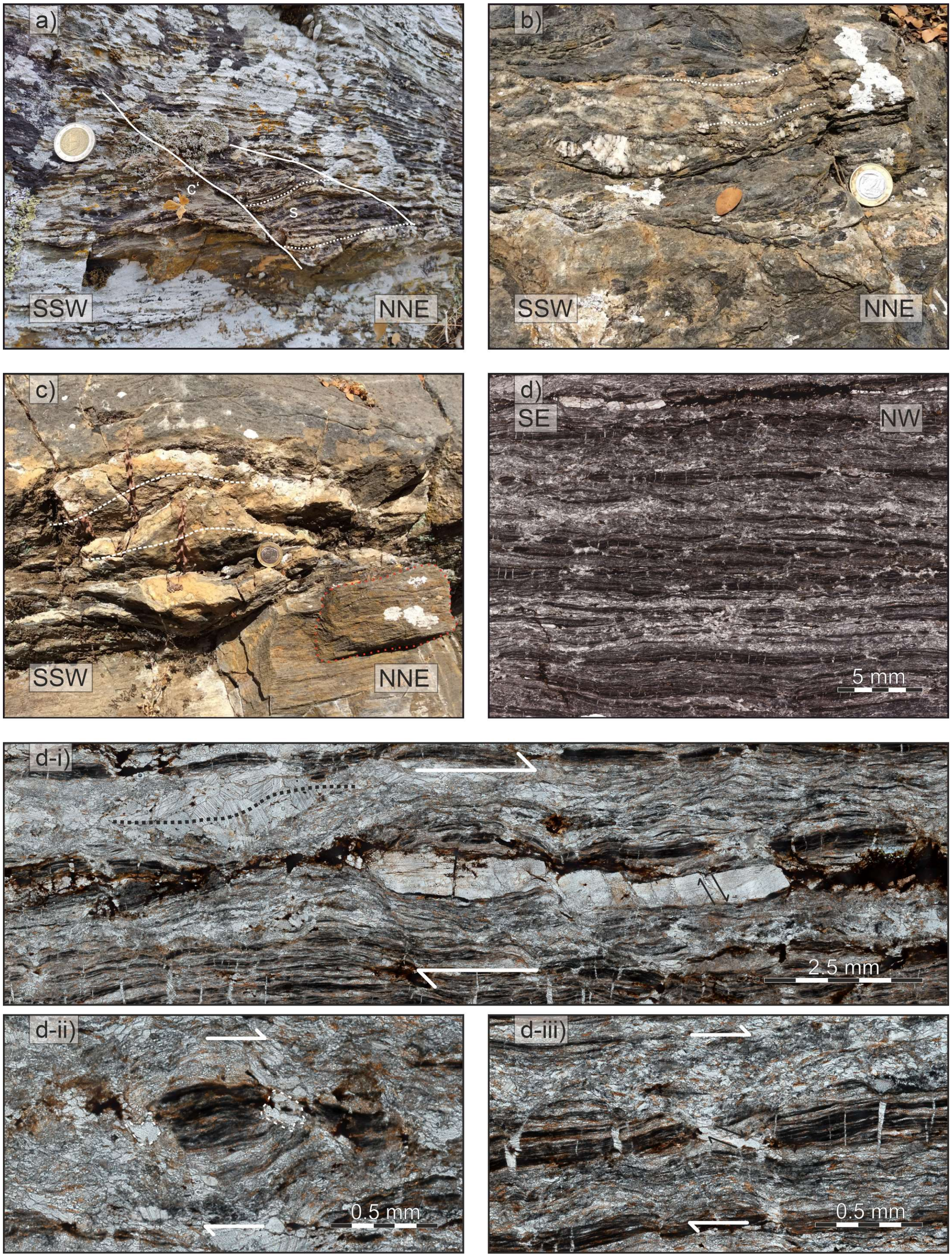

Figure 11: A representative marble of the Marina Basement Unit with characteristic structures. (a) Dark and well layered marble with a SCC' fabric. (b) The marble shows some sigmoids. White dashed lines trace the median line of the clast. Beneath those a quartz nodule is embedded in the marble (c). More sigmoids and joints cut the foliation. A red dotted line marks the in-situ specimen KZ-13. (d) Thin section scan (PPL) of a dominant foliated impure marble. Small calcite veins with an ataxial growth cutting the layers vertically to foliation. Photomosaics (PPL): (d-i) A calcite sigmoid with a black dashed median line and an asymmetric shear band boudinage. (d-ii) An impure calcite layer shows an asymmetric shear band boudinage, with marked boudin necks. (d-iii) A close-up of a shear band. All kinematics indicate a Top-to NNE shear sense. (KZ-13; 519848E, 4077807N)

The Marina Basement Unit contains metasediments, which lack any skarn minerals. There are quartz-rich biotite schists (Fig. 12) showing many isoclinal folds (f1). All isoclinal folds are aligned with the folded main foliation. A flanking fold structure and an asymmetric shear band boudinage are shown in Figures: (Fig. 12b&b-i).

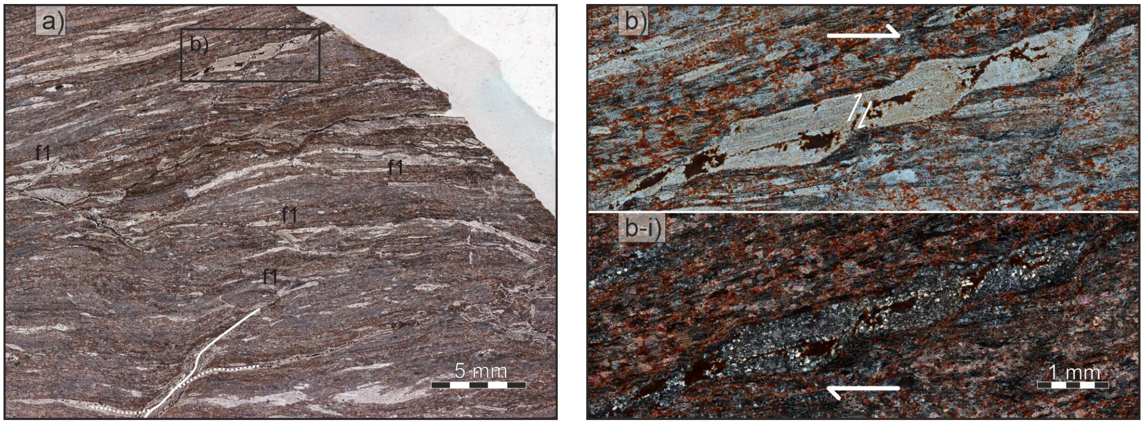

Figure 12: (a) Thin section scan (XPL) illustrates a biotite schist with many isoclinal fold hinges of the f1-fold generation, which are defined by quartz layers. In the mid-bottom is a flanking fold structure. This sample was collected as a loose hand sample. Therefore, the kinematics of this section could not be resolved. The black box indicates the position of the detailed figure. (b) Photomosaic (PPL/XPL) of an asymmetric shear band boudinage with a dextral shear sense. (K-267; a, b; 517476E, 4076124N)

During fieldwork well preserved and undeformed nummulites in a dark limestone were found in the Marina Cover Unit (Fig.13).

In one sample (K-352), a quartzitic layer has been deformed into a winged inclusion. The wings are surrounded by biotite, amphibolite and quartzite with a shape preferred orientation (SPO) along the foliation. The tint plate reveals a crystallographic preferred orientation of quartz at an angle of 30° to the foliation (Fig. 14d i-iii).

Figure 13: Dark nummulitic limestone; UTM35S: 517911/4077128

Directly at the contact of the intrusion, close to it on top of the mountain ridge, and on the northern slopes of Mt. Dikeos, quartzites and mica schists have been mapped. The sections show well foliated rocks, composed of quartz, feldspar, biotite, and garnet porphyroblasts (Fig. 16). Many of those garnets reveal a symplectitic structure along the rim (Fig. 14 a-c i-iii). One garnet porphyroblast exposes an inclusion-fabric zoning, because of an inclusion free core (Fig.XX b i-iii).

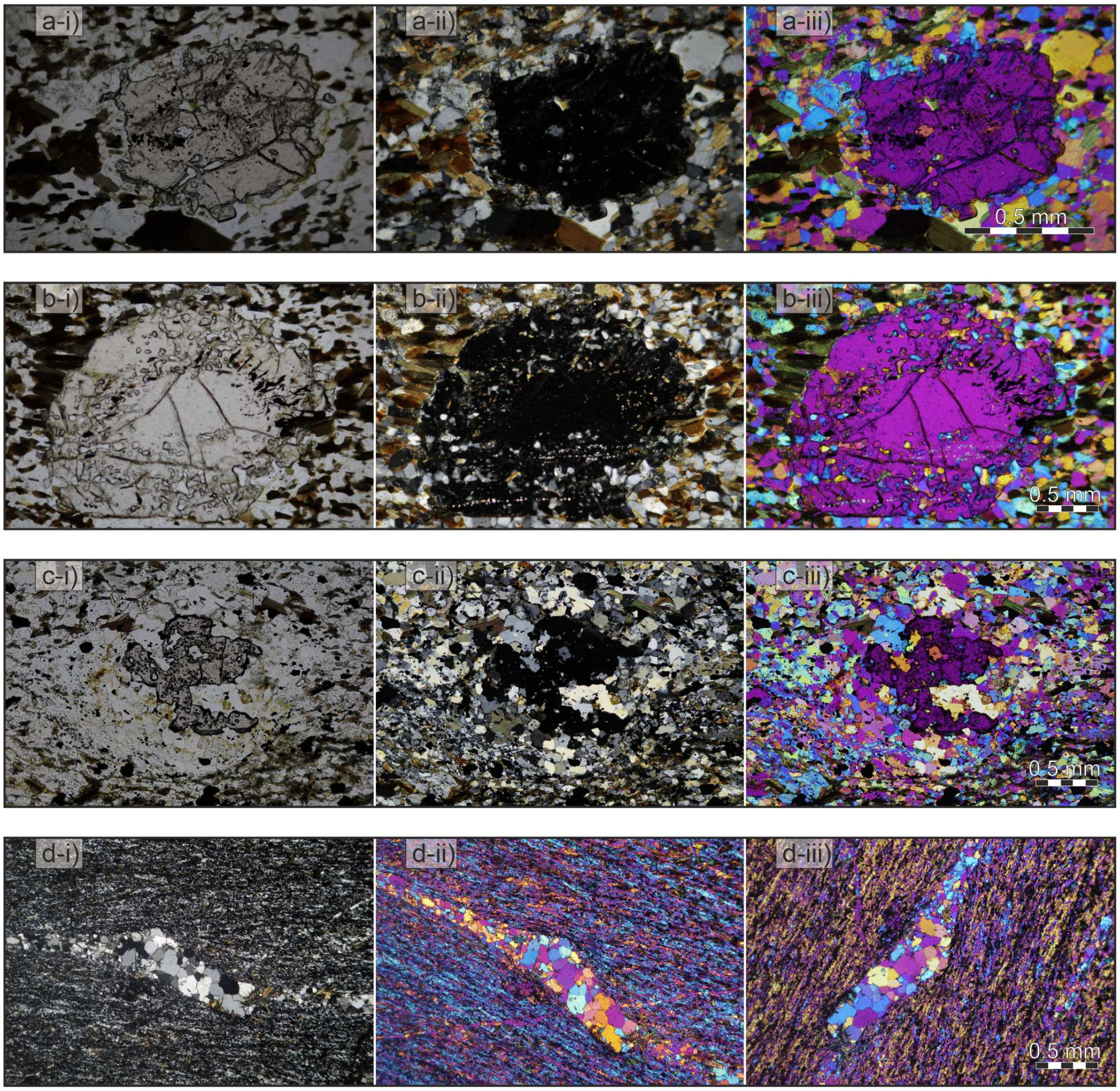

Figure 14: Photomicrographs of decomposed rotated garnet clasts and a winged inclusion. Photomicrographs of thin sections (PPL/XPL/XPL+lamda-shift): The figures of a, b & c show garnet porphyroblasts, which rotated in a foliated matrix of a garnet-biotite schist. (a) The garnet reveals symplectitic reactions around the blast (KK-4; 10x mag.). (b) This garnet has an unusual inclusion free core and was therefore analyzed by the EMPA (KK-4; 5x mag.). (a, b; 516952E, 4074529N) (c) Garnet remnants still show the augen structure with characteristic strain shadows (KZ-9; 5x mag.; c; 517609E, 4076250N) (d-i) A quartz layer forms a pinch and swell structure, including a winged inclusion, which started to rotate clockwise. (XPL; K-352; 5x mag.) (d-ii & d-iii) The matrix contains small grains of biotite, amphibolite, and quartz with a SPO aligned to the foliation and quartz with a CPO 45° to the foliation. Showing a dextral basal c slip (XPL+lamda-shift; K-352; 5x mag.; d; 517787E, 4075128N)

4.2. Petrologic analysis

4.2.1. Electron Microprobe data

For the petrological analysis, garnets from an endoskarn derived from monzonite, as well as garnets from metasedimentary rocks of the Marina Basement Unit, were examined. The endoskarn consists of polygonal pyroxene, garnet, plagioclase, and occasionally calcite and quartz, and it overprints a fold structure (Fig. 15a). At the base of the skarn zone, equigranular quartz and plagioclase grains are transected by the endoskarn along the axial plane of the fold. The relatively fine-grained minerals are overgrown by clinopyroxene. Near the fold hinge, garnet exhibits distinct polygonal zoning (Fig. 15b). The variation in the z-value is attributed to the formation of hydrogrossular within grossular.

Electron microprobe analyses (EMPA) were performed on garnet, biotite (in two samples), and ilmenite (in one sample) from six distinct samples. Sample KK-1 contains a minor proportion of hydrogrossular. To avoid influencing the average composition of garnets in the sample, this phase was excluded from the classification of other garnet types. Nevertheless, its compositional data is included alongside the other results in Table 1. Additional mineral phases analyzed include ilmenite and biotite.

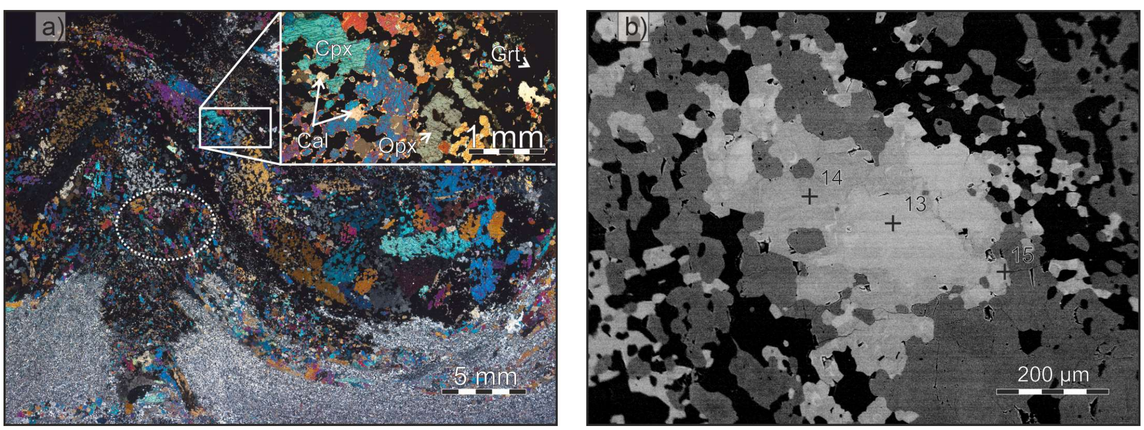

Figure 15: (a) A Thin section scan (XPL) of an endoskarn overgrows a fold shape. The dashed ellipse indicates the location of the BSE image (b). (b) The zoned phases with a relatively high z-value depict the garnet (Hgrs), a medium z-value is pyroxene, and a low z-value are quartz and plagioclase. Marked symbols indicate point measurements of the EPMA (KK-1; a, b; 515429E, 4074386N).

	KZ - 9	KZ - 11		KZ - 18		KK - 1		KK - 3		KK - 4
	Grt	Grt	Ilm	Grt	Bt	Grt	Hgrs	Grt	Ilm	Grt
wt% oxides										
SiO_2	36.9	37.4	0.0	36.4	33.7	38.5	34.8	36.9	0.0	36.7
MgO	2.0	3.7	0.0	1.6	4.3	0.2	1.9	1.9	0.1	1.8
Cr_2O_3	0.1	0.0	0.0	0.1	n.m.	0.0	0.1	-0.0	0.1	0.0
TiO_2	0.1	0.1	52.6	0.1	2.5	0.6	3.5	0.1	53.2	0.1
CaO	1.2	2.2	0.0	0.8	0.0	34.5	33.7	0.7	0.0	1.0
MnO	1.3	0.8	0.6	1.1	0.0	0.3	0.0	2.2	0.3	2.3
Al_2O_3	20.5	20.8	0.0	20.4	19.3	16.9	13.3	20.3	0.0	20.3
FeO	38.2	35.1	46.6	39.4	25.5	8.5	4.8	38.1	46.5	37.9
Na_2O	n.m.	n.m.	0.0	n.m.	0.2	n.m.	n.m.	n.m.	0.2	n.m.
K_2O	n.m.	n.m.	0.0	n.m.	8.6	n.m.	n.m.	n.m.	0.0	n.m.
F	n.m.	n.m.	0.0	n.m.	0.2	n.m.	n.m.	n.m.	0.0	n.m.
BaO	n.m.	n.m.	n.m.	n.m.	0.2	n.m.	n.m.	n.m.	n.m.	n.m.
OH	n.m.	n.m.	n.m.	n.m.	n.m.	n.m.	0.1	n.m.	n.m.	n.m.
Total	100.15	100.15	100.01	99.77	94.52	99.53	100.0	100.2	100.49	100.1
Normalized to oxygens										
Si	3.00	2.99	0.00	2.98	2.76	2.97	2.89	3.00	0.00	2.99
Mg	0.24	0.44	0.00	0.20	0.53	0.02	0.25	0.23	0.00	0.22
Cr	b. d.	0.00	0.00	0.01	n.m	0.00	0.00	0.00	0.00	0.00
Ti	0.01	0.00	1.00	0.01	0.16	0.04	0.22	0.01	1.00	0.00
Ca	0.10	0.19	0.00	0.07	0.00	2.87	3.00	0.06	0.00	0.09
Mn	0.09	0.05	0.01	0.07	0.00	0.02	0.00	0.15	0.01	0.16
Al	1.96	1.96	0.00	1.97	1.87	1.54	1.30	1.95	0.00	1.96
Fe^{2+}	2.60	2.35	n.c.	2.64	0.51	0.12	n.c.	2.56	n.c.	2.53
Fe^{3+}	0.00	0.00	n.c.	0.05	1,24	0.42	0.33	0.03	n.c.	0.05
Fe_{tot}	2.60	2.35	0.98	2.69	1.75	0.54	0.33	2.59	0.97	2.58
Na	n.m.	n.m.	n.m.	n.m.	0.04	n.m.	n.m.	n.m.	n.m.	n.m.
K	n.m.	n.m.	0.00	n.m.	0.90	n.m.	n.m.	n.m.	0.01	n.m.
F	n.m.	n.m.	0.00	n.m.	0.00	n.m.	n.m.	n.m.	0.00	n.m.
Ba	n.m.	n.m.	n.m.	n.m.	0.01	n.m.	n.m.	n.m.	n.m.	n.m.
OH	n.c.	n.c.	n.c.	n.c.	2.00	n.c.	0.1	n.c.	n.c.	n.c.
Total	8.00	8.00	2.00	8.00	8.00	8.00	7.99	8.00	2.00	8.00

Table 1: The average phase compositions of the six selected samples; Grt: 12 O, Fe^{3+} per charge balance; Bt: 12 O, 2 OH, Fe^{2+}/Fe^{tot} = 0,29; Ilm: 3 O 2 cations normalized to 2 oxygens; Abbreviations: n.m.: not measured; n.c.: not calculated b. d.: below detection limit

4.2.2. Garnet types and microstructural context

The microstructural fabric of the various thin sections containing garnet differs significantly. It ranges from amoeboidal garnet growth in the endoskarn (KK-1) and in the mylonitic Grt-Bt-Chl schist (KZ-11), to coarse-grained garnet porphyroblasts (KZ-9, KK-3, KK-4), and garnet relicts within a Qz-Bt-Scp-And hornfels (KZ-18) (Fig. 16). Notably, sample KZ-11 lacks typical skarn minerals such as andalusite, cordierite, scapolite, or wollastonite. Some garnet domains of KK-1 and KZ-11 contain minor amounts of hydrogrossular. Hypidiomorphic garnet porphyroblasts (KZ-9, KK-3, KK-4) appear to flow or rotate within the matrix and often contain numerous inclusions, particularly quartz.

The garnet–biotite schists of KK-3 and KK-4 exhibit sericitized feldspars and garnets with symplectitic structures at their rims. In thin section KK-3, a chain of garnets is relatively well aligned with a weak foliation, later crosscut by a vertical brittle fracture. KK-4 and KZ-9 display a more pronounced foliation than KK-3, differing in porphyroblast size and evidence of precipitation processes. The Grt-Cor-Qz schist of KZ-9 contains poikiloblastic garnets up to 3 mm in diameter, with biotite layers aligned along the foliation that bend around the garnet grains. These layers are concentrated in the middle horizontal section, where ilmenite dominates. The garnets show 100-800 µm large quartz inclusions, some of which are even elongated. Sample KZ-18 features a variety of typical skarn porphyroblasts composed of andalusite, cordierite, scapolite, decomposed garnet, and ilmenite grains distributed throughout the thin section. The fabric of the grains is best described as poikiloblastic. Black trails of fine-grained material and voids follow a slightly curved foliation. All thin sections exhibit subgrain rotation (SGR) and polygonal grain boundaries of quartz and plagioclase to varying degrees.

The analyzed garnets are predominantly composed of almandine (83%), with minor components of pyrope (9%), spessartine (4%), and grossular plus andradite (4%) (Fig. 17). Sample KZ-11 shows a slightly elevated andradite content (4–6%). The endoskarn (KK-1) is an exception, with a composition dominated by grossular (73%), andradite (19%), and almandine (3%). Due to the high titanium content, titanium-rich garnet species such as melanite and schorlomite (approximately 3.5%) are also present.

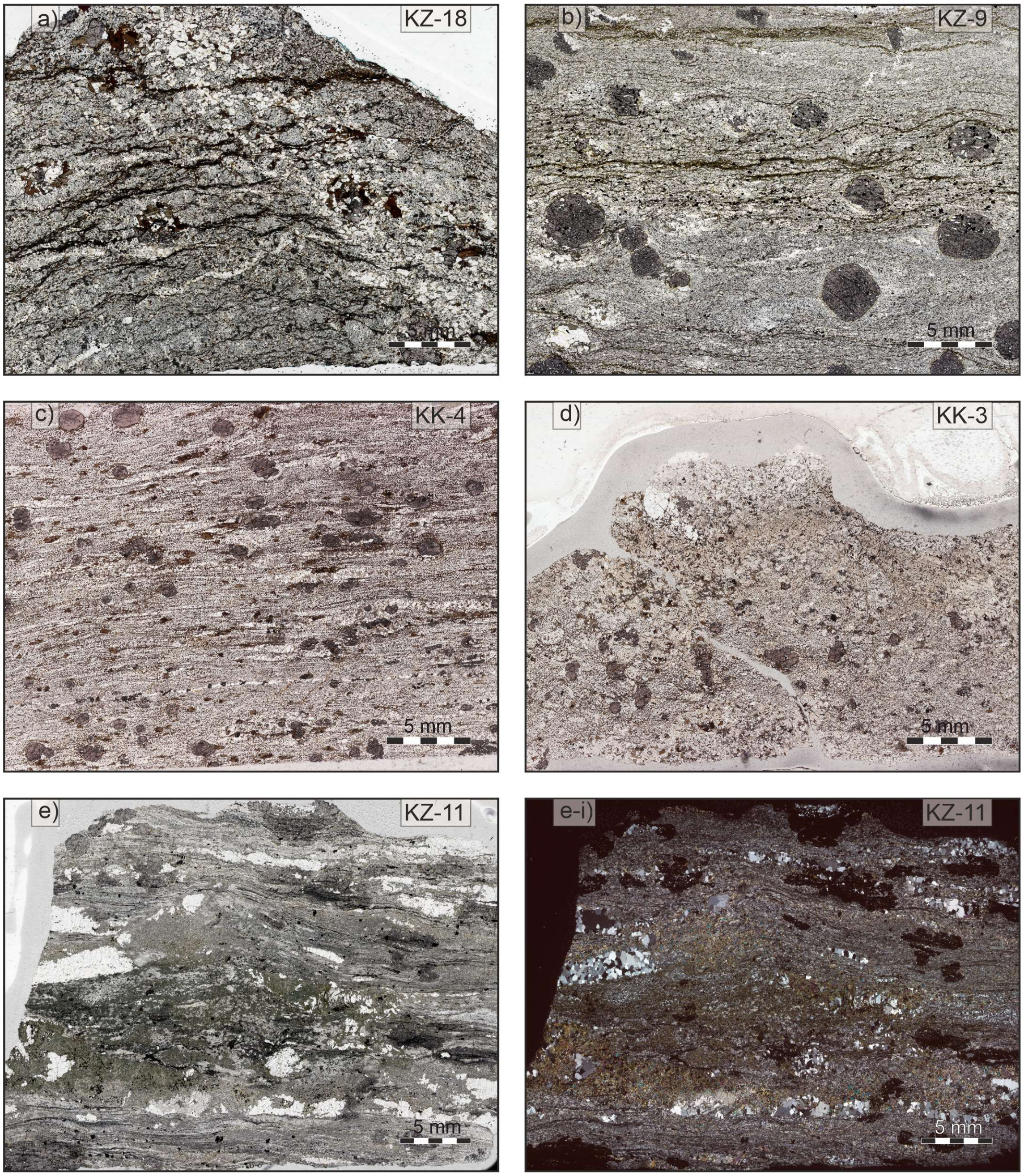

Figure 16: All different non-endoskarn garnet populations, which were found in the Marina Basement Unit during fieldwork are displayed. (a) Thin section scans (a-f/PPL; a-i/XPL): (a) Hornfels fold core that is full of cordierite and some andalusite nodules. Garnets are decomposed into quartz and plagioclase, and a dominant solution cleavage that follows the folded foliation (KZ-18; 517541E, 4076116N). (b) Garnet-biotite schist with up to 3 mm large, rotated garnet clasts (KZ-9; 517609E, 4076250N). (c) Garnet-biotite schist with a dominant foliation and some decomposed garnets (KK-4; 516952E, 4074529N) (d) Garnet-biotite schist of a fold core (KK-3; 516952E, 4074529N) (e & e-i)) Garnet-mica schist with elongated garnet and Qz aggregates KZ-11 (517609E, 4076250N).

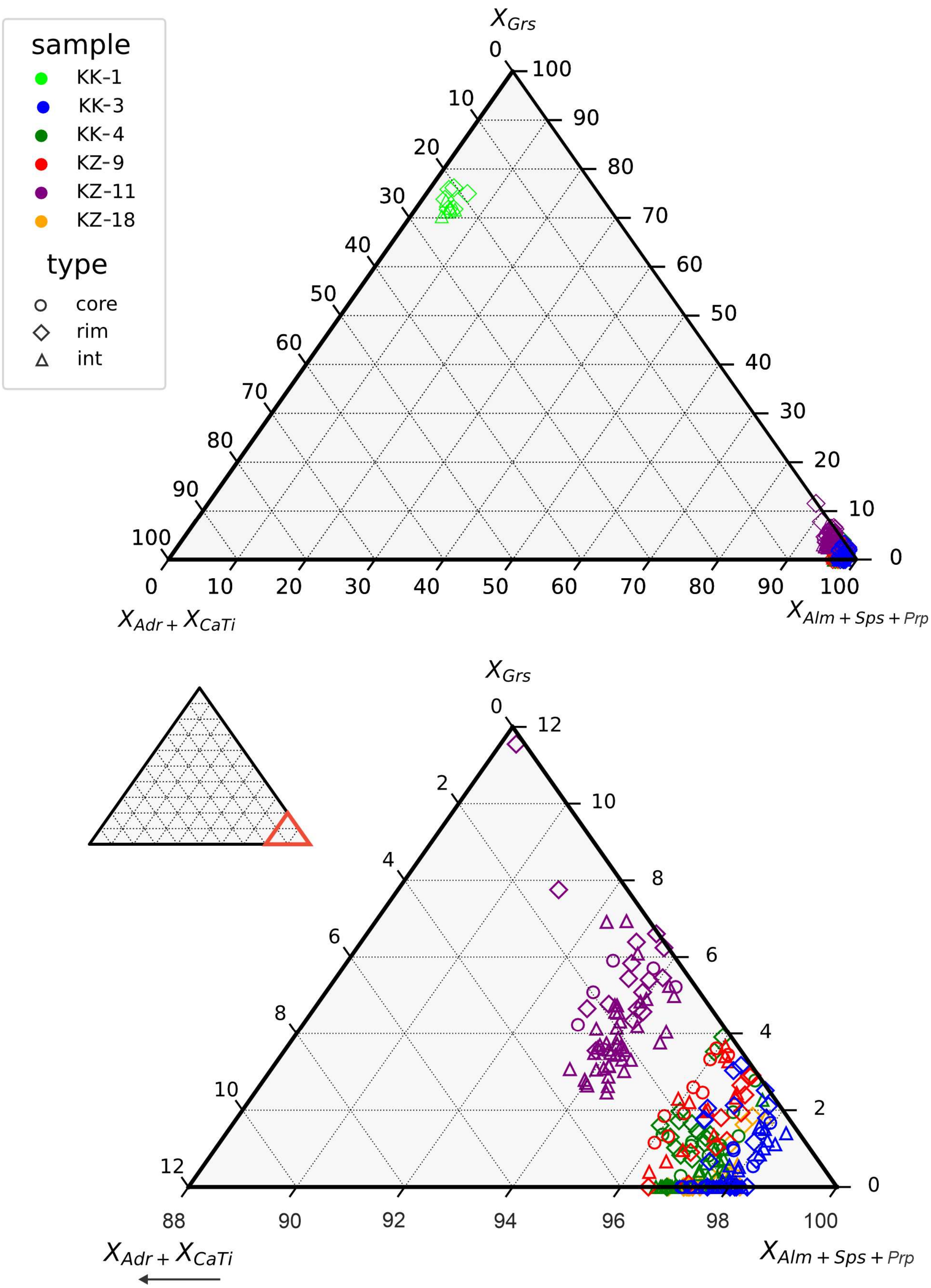

Figure 17: Triangular plots of mineral chemistry analyses from all measured garnet species (a) Triangular plot of endmember fractions XAdr+XCaTi - XGrs - XAlm+XSps+XPrp. Colors correspond to different samples, and the symbol shape relates to an approximate location of the point measurement in the Grt phases as given in the key. (b) To highlight the different garnet species of the Marina Basement Unit endmember fractions, the plot shows the bottom right corner with XAlm+XSps+XPrp (88 to 100% as marked in the sketch).

A plot of Mg-number MgO/(MgO+FeO) versus silicon content reveals a similarity among almandine-rich samples, particularly KK-3, KK-4, and KK-9 (Fig. 18a). KZ-18 shows a slightly lower Mg-number, though still overlapping with the aforementioned samples. KZ-11 displays a similar distribution to the other almandines but trends toward the grossular-rich composition of KK-1, which exhibits a more scattered Mg-number. The Mg-number depicts a range of 0.06 to 0,18. The $Fe^{2+}/(Fe^{2+}+Mg)$ ratios of garnets from this study are between 0.82 to 0.94, with no significant difference between the rim and the core. A plot of total iron content versus calcium shows a comparable pattern to the Mg-number plot (Fig. 18b). A difference in calcium content of KK-3 and KK-4 compared to KZ-9 is highlighted. KZ-18 has a higher iron content, indicating a greater almandine component. In contrast, garnets from KZ-11 are lower in iron and higher in calcium, suggesting a compositional transition toward the grossular-rich endoskarn.
In three different samples (KK-3, KK-4, and KZ-11), four profile lines were measured from the rim to the core of garnet porphyroblasts (Fig. 19). The locations and orientations of these profiles are shown in BSE images of the garnets. Large, relatively inclusion-free clasts were selected for analysis. Both garnet porphyroblasts in sample KK-3 contain ilmenite in cores, while the garnet in KK-4 exhibits inclusion-fabric zoning visible under polarized light microscopy.
The profiles reveal a relatively constant garnet composition over the measured distance (Fig. 20a). Only sample KZ-11 shows slight irregularities in grossular and calcium content. For all garnet samples excluding KK-1, the plot of calcium and manganese concentrations against profile distance indicates an inverse relationship (Fig. 20b). On the path to the core, manganese increases while calcium remains stable or decreases slightly. The absolute content of manganese and calcium of the profile KZ-11 compared to the other profiles (KK-3 & KK-4) is swapped. The spatial distribution of manganese in KZ-11 is markedly more heterogeneous and the rim contains more manganese than that observed in the other profiles.

Iron and manganese content plotted against profile distance shows a generally steady or slightly increasing trend (Fig. 21a). The Mg-number plotted against profile distance reveals a minor decrease toward the core (Fig. 21b).

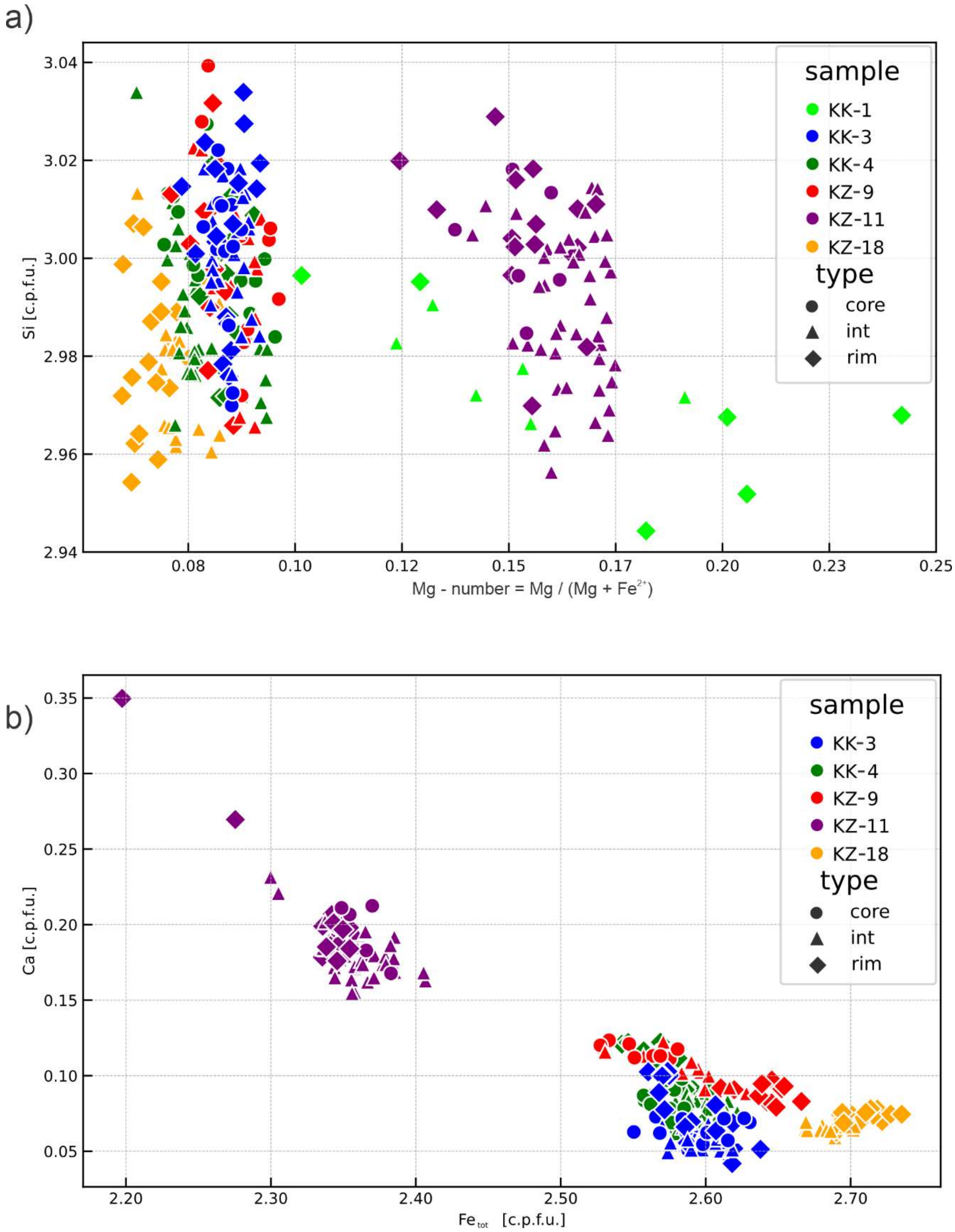

Figure 18: Binary plots of the various color-coded garnet samples with different measurement location symbols as given in the key. (a) Mg-Number - Si [c.p.f.u.]. (b) Fe_{tot} [c.p.f.u.] - Ca [c.p.f.u.] ($Fe_{tot}=Fe^{2+}+Fe^{3+}$) - sample KK-1 is excluded.

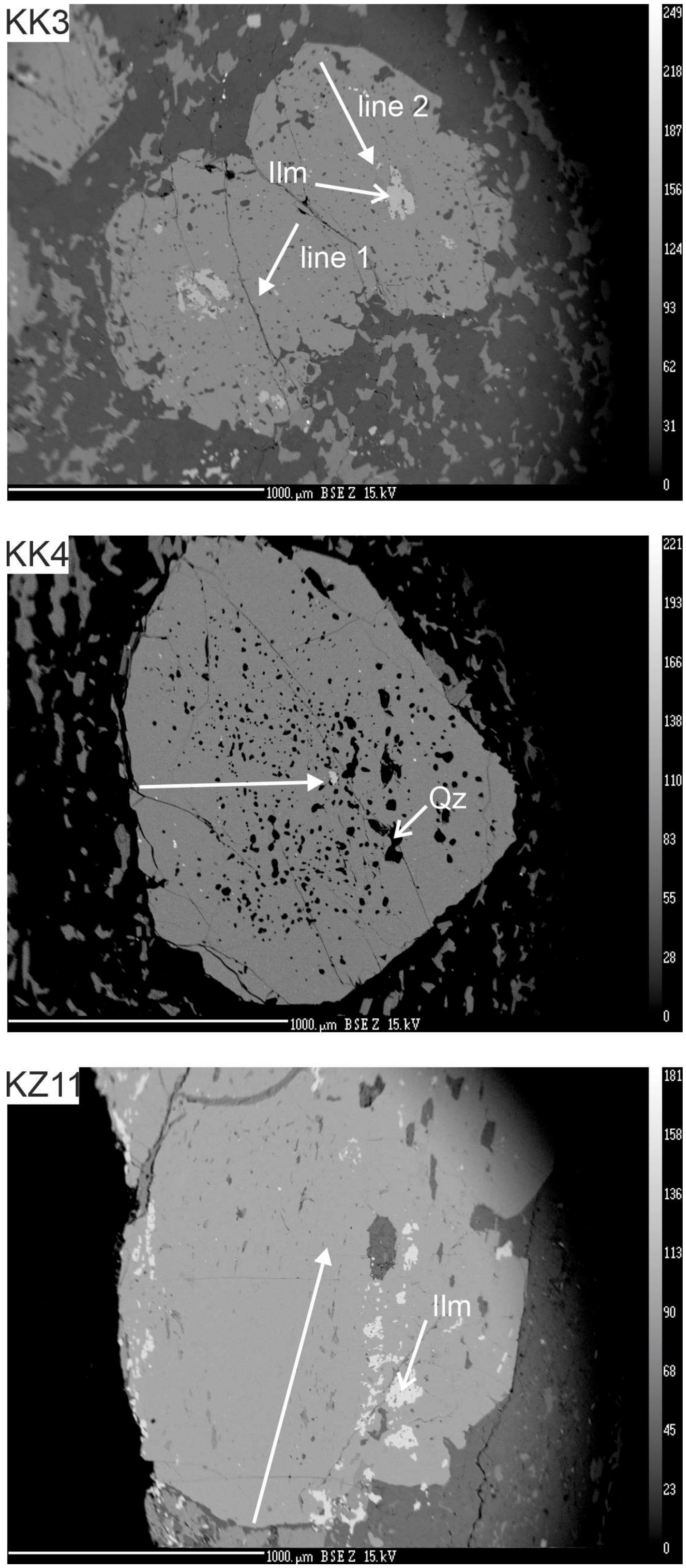

Figure 19: BSE images of measured garnet (KK3, KK4, KZ11; EPMA) indicating the line profile name, location and acquisition direction. The inclusions consist primarily of quartz and ilmenite.

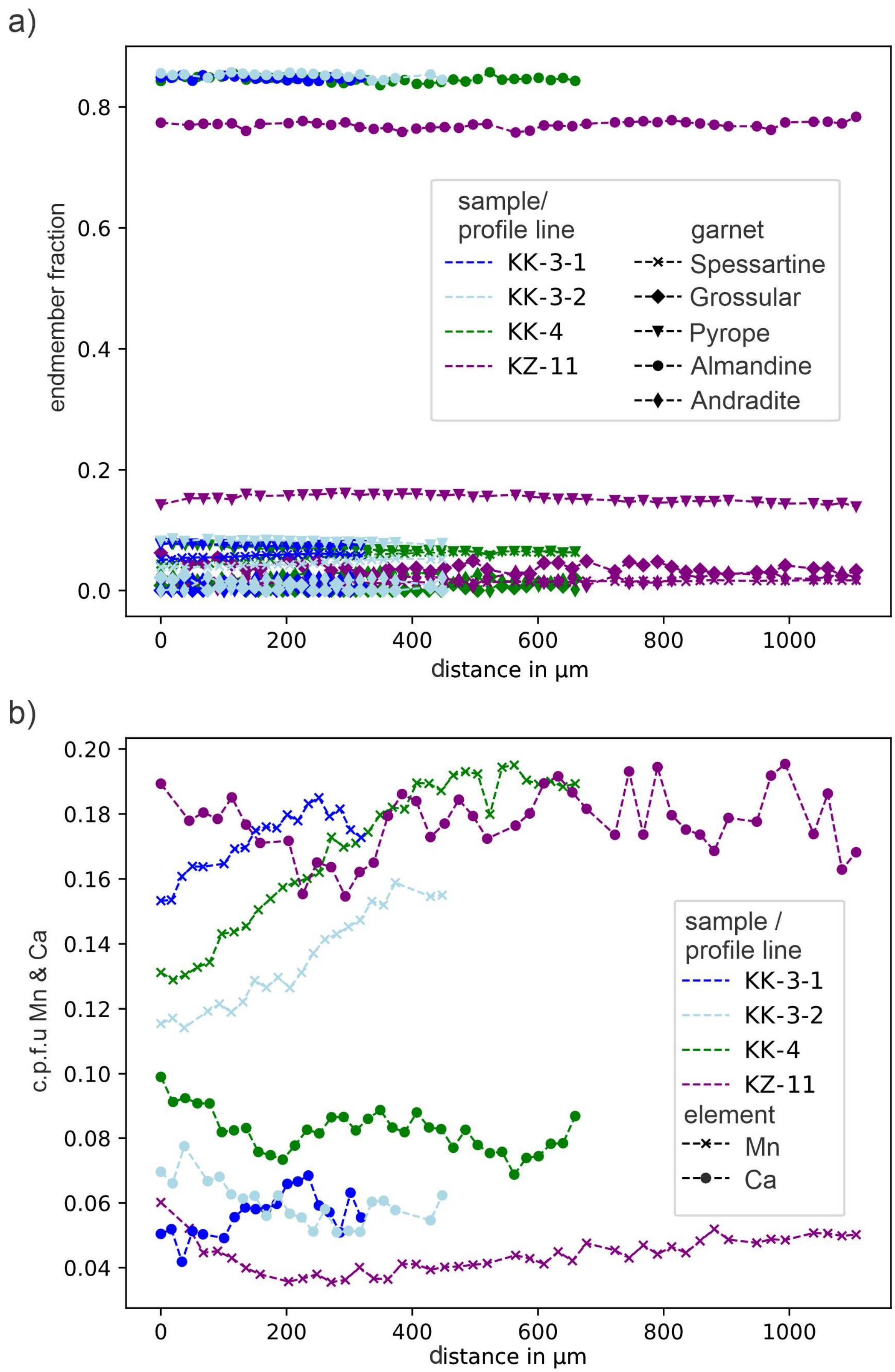

Figure 20: Garnet composition along measured profiles (a) Distance in µm plotted versus endmember fractions of garnets. (b) Distance in µm plotted versus element fraction (c.p.f.u Mn &Ca) of garnets. x for X_{Mn} and dots for X_{Ca}.

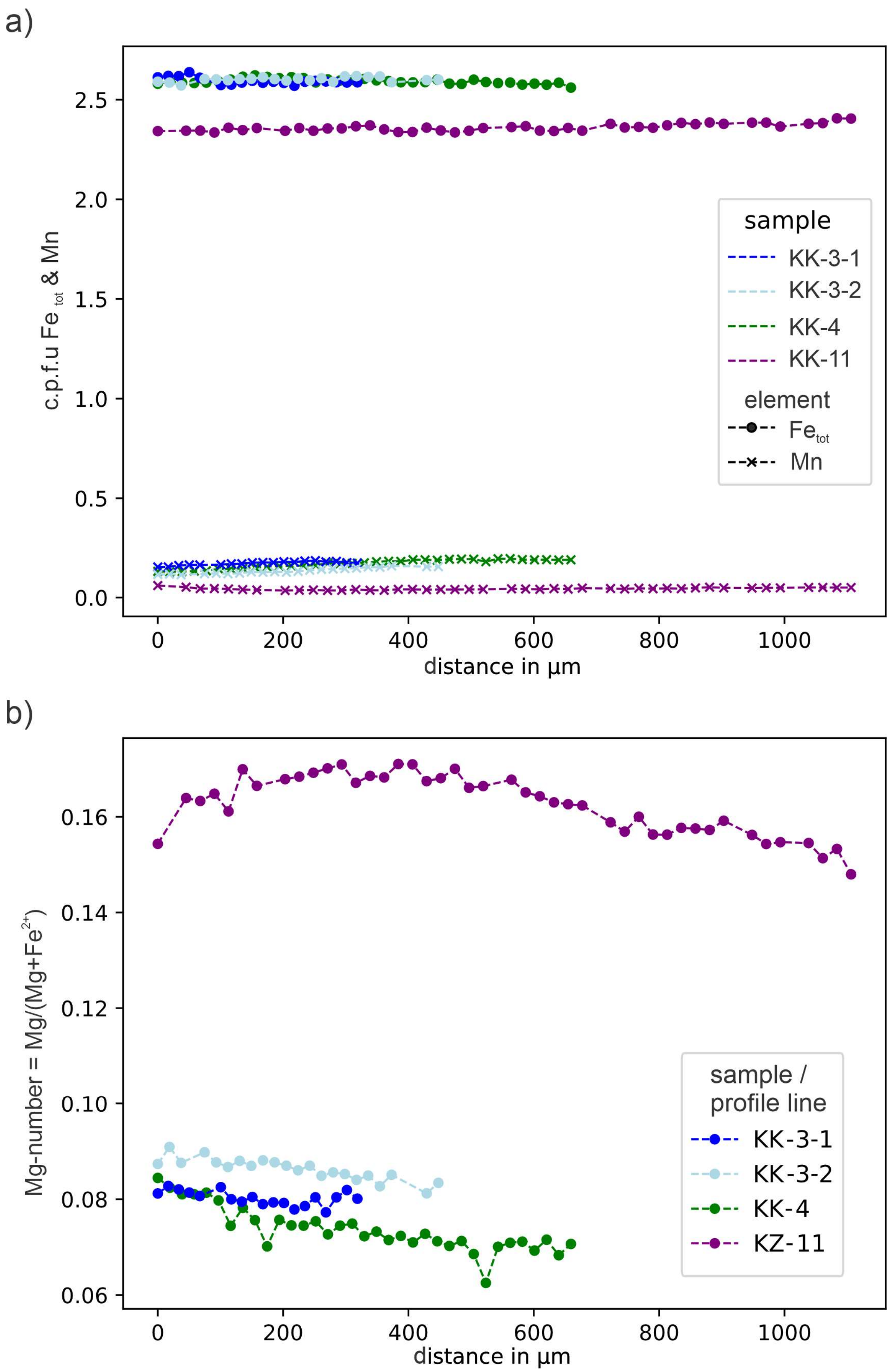

Figure 21: Garnet composition along measured profiles (a) Distance in µm plotted versus element fraction (c.p.f.u Fe_{tot} & Mn) of garnets. x for X_{Mn} and circle for X_{Fe} (b) Distance in µm plotted versus Mg-Number of garnets.

4.2.2.1. Biotite

Biotite phases of the sample KZ-18 were checked for their composition based on their position. They show no systematic differences between grains in contact with garnet or in the matrix (Fig. 22).

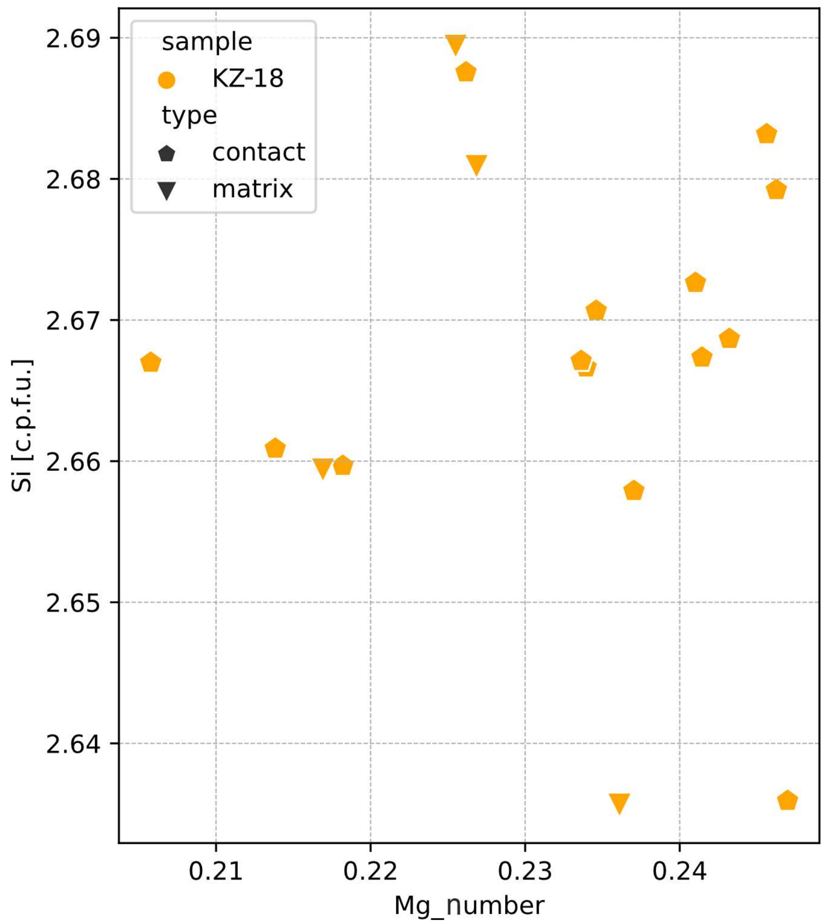

Figure 22: Mg-Number - Si [c.p.f.u.] plot for biotite of the sample KZ-18. The pentagon symbol indicates a proximity to or phase boundary with garnets and triangles represent matrix biotite phases.

4.2.2.2. Ilmenite

Ilmenite has a minor substitution of Fe^{2+} by Mg (Geikelithe) and Mn (Pyrophanite), but the ilmenite phases are quite similar in their composition in all samples where they were measured (Fig. 23).

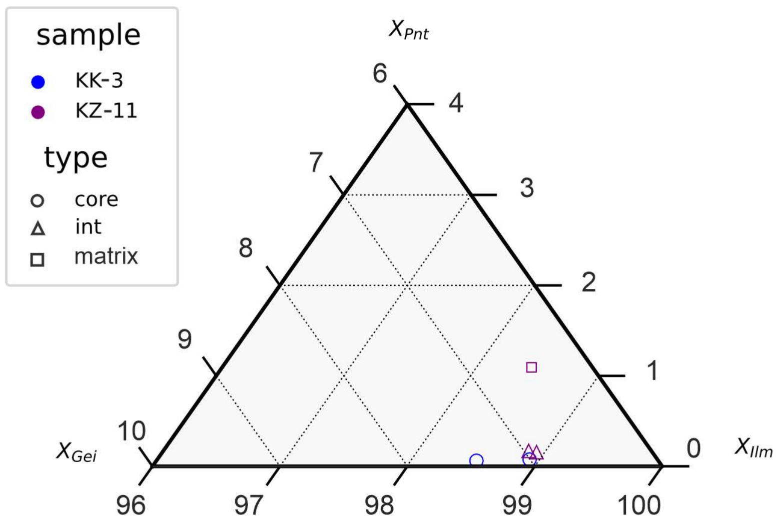

Figure 23: A Triangular plot of mineral chemistry analyses from two samples of ilmenite of different areas in relation to garnets is illustrated.

4.2.3. Scanning electron microscope (SEM)

The quartz-mica mylonite of sample K-352 shown below was selected for SE, BSE, CL imaging, and EDX analysis on four marked sites (Fig. 24). The upper and lower sections, characterized by brownish and greenish color tones, contain higher amounts of amphibole and chlorite with a decussate texture, in contrast to the central section, which is dominated by quartz that exhibits subgrain rotation (SGR). The opaque phases are identified as ilmenite. Pinch and swell structures are present in the upper and lower parts of the sample; however, only one pinch of each structure is visible. In the central area, a quartzitic layer contains winged inclusions (see Chapter 4.1.1, Fig. 14d i-iii). As observed in all mica schists of the unit, isoclinal folds (f1) are present. A kink band deforms all layers within the thin section. Sharp veins, parallel to the kink band and filled with chlorite and quartz, cross the entire section. Some layers contain deformed aggregates that served as focal points for SE, BSE, and CL imaging.

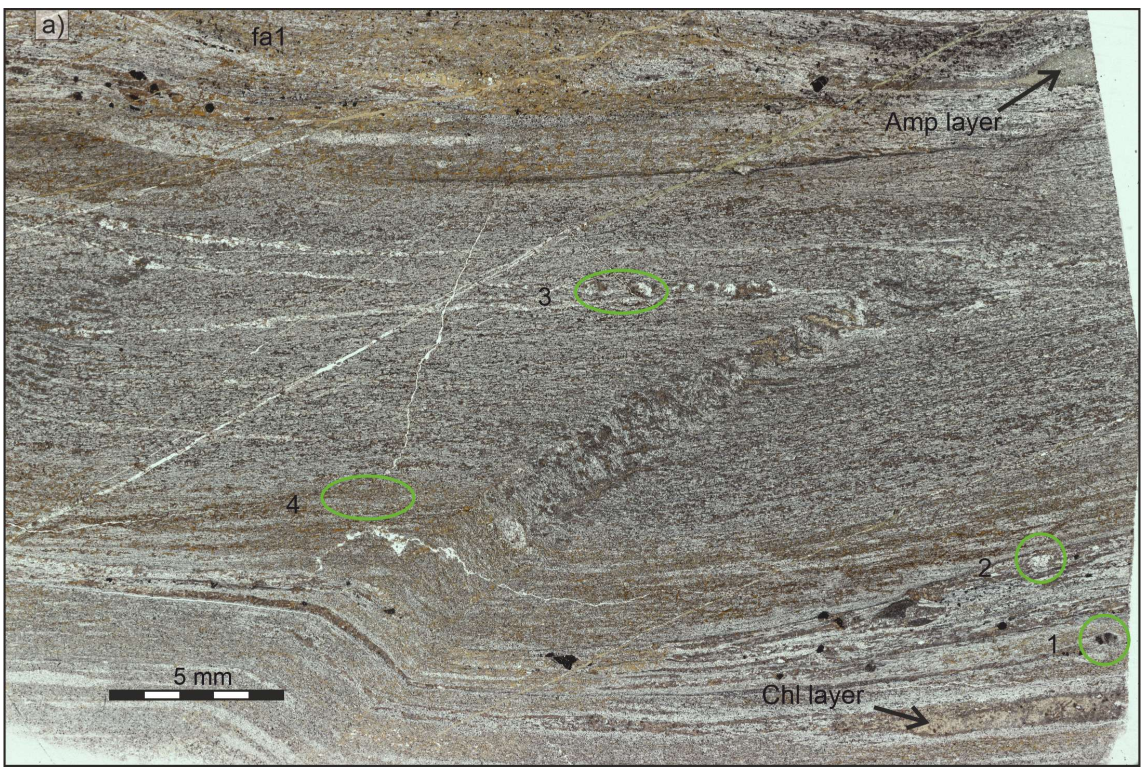

Figure 24: (a) Thin section scan (PPL) of a mylonitic biotite schist composed of quartz, plagioclase (mostly oligoclase); (K-352; 517787E, 4075128N). In addition, one chlorite and one amphibole marked layer. A dominant kink band crosses the hole section, and a fa1 isoclinal fold is visible in the top left corner. Green ellipses mark areas where BSE, SE, and CL images were taken.

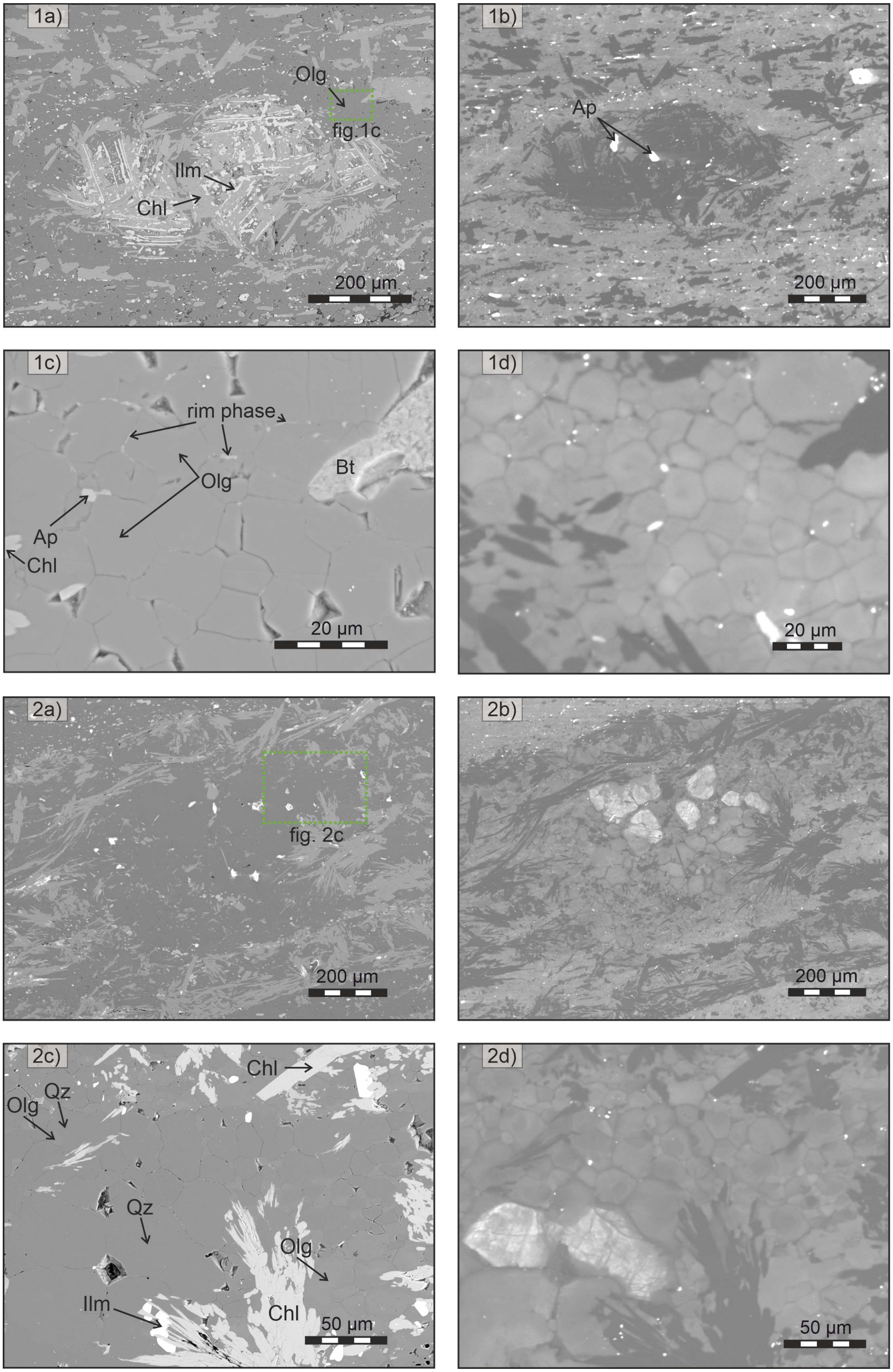
1a)
Olg
fig.1c
Ilm
Chl
200 µm
1b)
Ap
200 µm
1c)
rim phase
Olg
Bt
Ap
Chl
20 µm
1d)
20 µm
2a)
fig. 2c
200 µm
2b)
200 µm
2c)
Chl
Olg
Qz
Qz
Olg
Ilm
Chl
50 µm
2d)
50 µm

Figure 25: (1a) In area 1, a BSE picture depicts clast shaped aggregates of chlorite and sprayed ilmenite that are surrounded by oligoclase and some quartz. (1b) CL image of the same location reveals approximately 20-50 µm apatite clasts. The apatite is slightly distorted by persistent luminescence. (1c) SE image of the marked area in (1a). Polygonal oligoclase with a rim phase on the edges, which is composed of a manganese and iron silicate phase. (1d) CL image exposes zoned oligoclase phases. (2a) SE image of an aggregate of oligoclase and quartz surrounded by chlorite (2b) CL image reveals fractured quartz grains. (2c) BSE image of the marked green area with polygonal plagioclase & quartz, small ilmenite flakes, and elongated chlorite. (2d) CL image of 40-80 µm quartz grains.

At the first observation site, an aggregate of chlorite intergrown with ilmenite is present, exhibiting a fibrous microstructure that suggests a previously elongated porphyroblast shape. This structure is surrounded by a quartz-plagioclase-rich rim (Fig. 25-1a). The cathodoluminescence (CL) image reveals apatite that is otherwise obscured in SE or BSE imaging (Fig. 25-1b). At higher magnification, oligoclase and quartz exhibit polygonal grains with well-developed triple junctions. Chlorite and biotite, characterized by higher Z-values, display an elongated tabular grain shape. Between phase boundaries, a rim phase is present, consisting of a compositional mixture of all involved mineral species (Fig. 251c). At the same location, a CL image reveals concentric zoning within the plagioclase (Fig. 25-1d).

An aggregate of quartz and oligoclase with polygonal grain shapes is surrounded by fascicular and tabular chlorite in area 2 (Fig. 25-2a). CL imaging reveals quartz grains with high CL intensity and numerous internal fractures (Fig. 25-2b&d). Ilmenite grains and pores of varying sizes are distributed throughout the entire thin section (Fig. 25-2c).

In area 3, a monoclinal structure composed of polygonal quartz, oligoclase, and fascicular chlorite is observed (Fig. 26-3a&b). CL imaging indicates a compositional contrast between the structure and the surrounding matrix, particularly in terms of apatite content, which is lower within the structure. At higher magnification, CL images reveal tail-like extensions associated with these structures (Fig. 26-3c).

Site 4 consists of biotite, amphibole, quartz, plagioclase, as well as ilmenite, and the matrix displays brownish and greenish color domains (Fig. 26-4). Biotite is oriented approximately parallel to the horizontal foliation, whereas amphibole shows subhorizontal to vertical alignment.

Zoned plagioclase was analyzed using EDX, confirming the presence of compositional zoning. The plagioclase can be classified as oligoclase, with cores exhibiting elevated calcium and a slight decrease in potassium content. The difference is only a few weight percent, placing it within the compositional range between oligoclase and albite (Fig. 27).

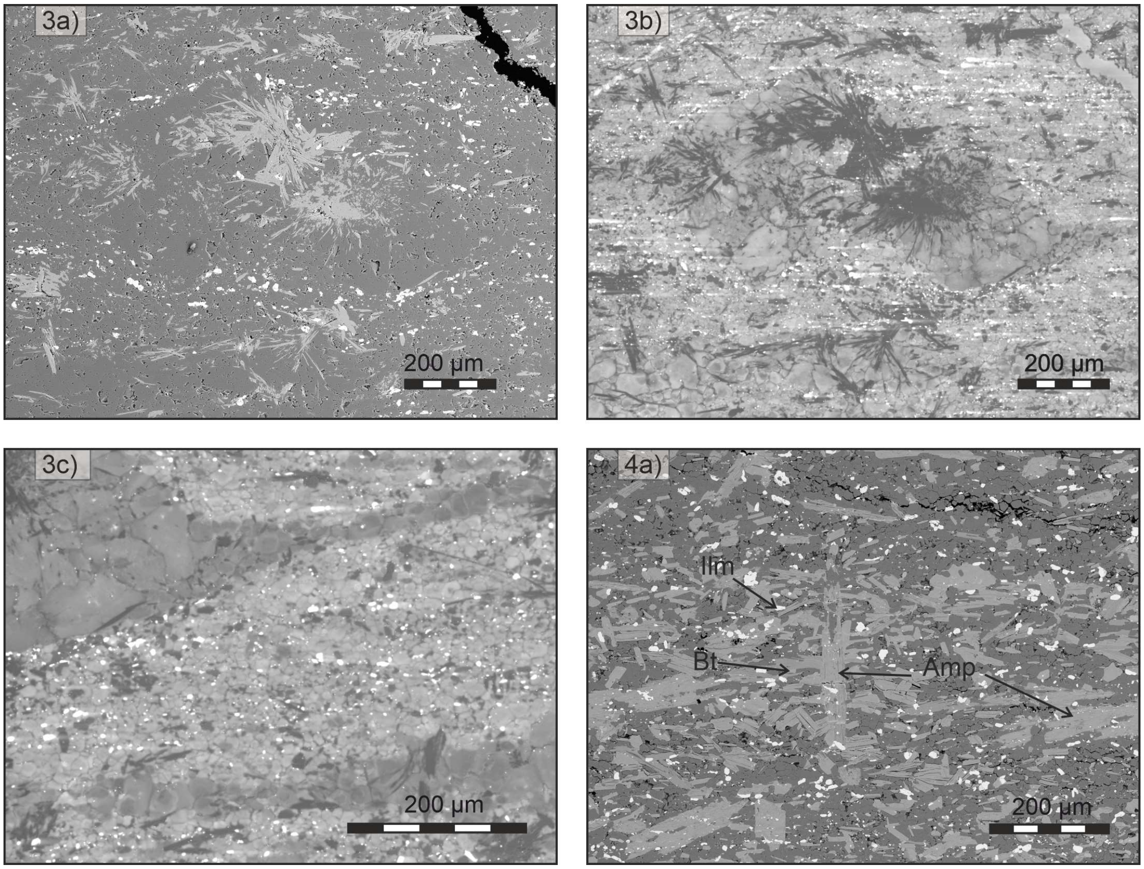

Figure 26: (3a) BSE image of area 3, ilmenite bends around an aggregate with polygonal quartz, oligoclase and chlorite. (3b) CL image exposes that the aggregate is sigmoid-shaped with quartz & plagioclase tails. (3c) CL image of a closeup from sigmoid tails with a lower z-value than the matrix. (4a) BSE image of area 4 is enriched in biotite. Larger amphiboles intersect with biotite.

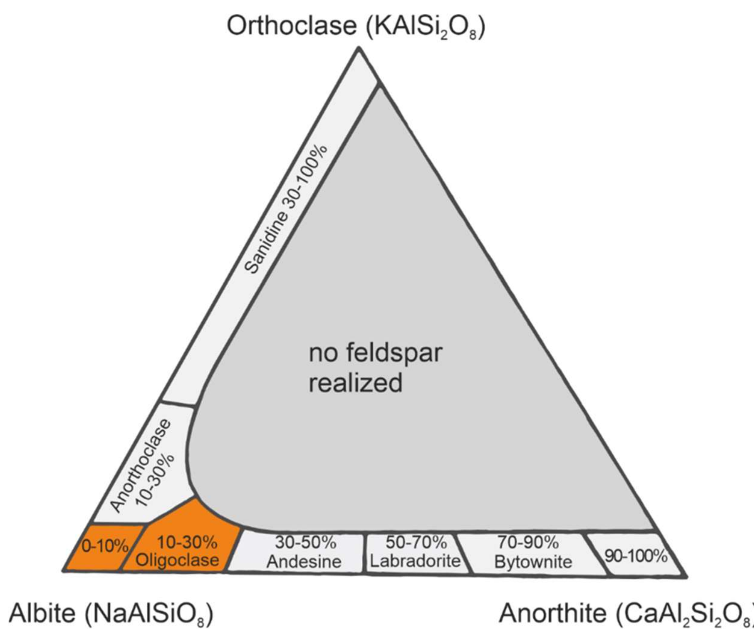

Figure 27: Feldspar compositional ternary diagram: The orange field marks the area where the composition of EDX point measurements of the feldspars locates

4.2.4. Raman spectroscopy of carbonaceous materials (RSCM)

For thermometric analysis using Raman spectroscopy of carbonaceous material, ten samples from the collected batch in this study were selected. These samples were chosen due to their relatively high content of carbonaceous material and their proximity to the Kos Pluton. The specimens primarily consist of graphite-bearing metapsammitic to metapelitic schists, including one graphite schist (KZ-14) located near the Dikeos peak. The RSCM temperatures obtained in this study, along with those reported by Roche et al. (2024), are shown on the thermometric map (Fig. 29), modified by Roche et al. (2024). Additionally, mineral isograds and calculated temperatures from Kalt et al. (1998) have been included.

For Raman spectroscopy analysis, 15 to 20 spectra per sample were collected, covering the spectral regions of the first and, where applicable, the second order. The latter was included in cases where the main S-band exhibited splitting, indicative of more highly ordered carbonaceous material (CM), predominantly graphite. The waterfall chart (Fig. 28) below illustrates representative spectra from various samples, showing both 1. and 2. order.

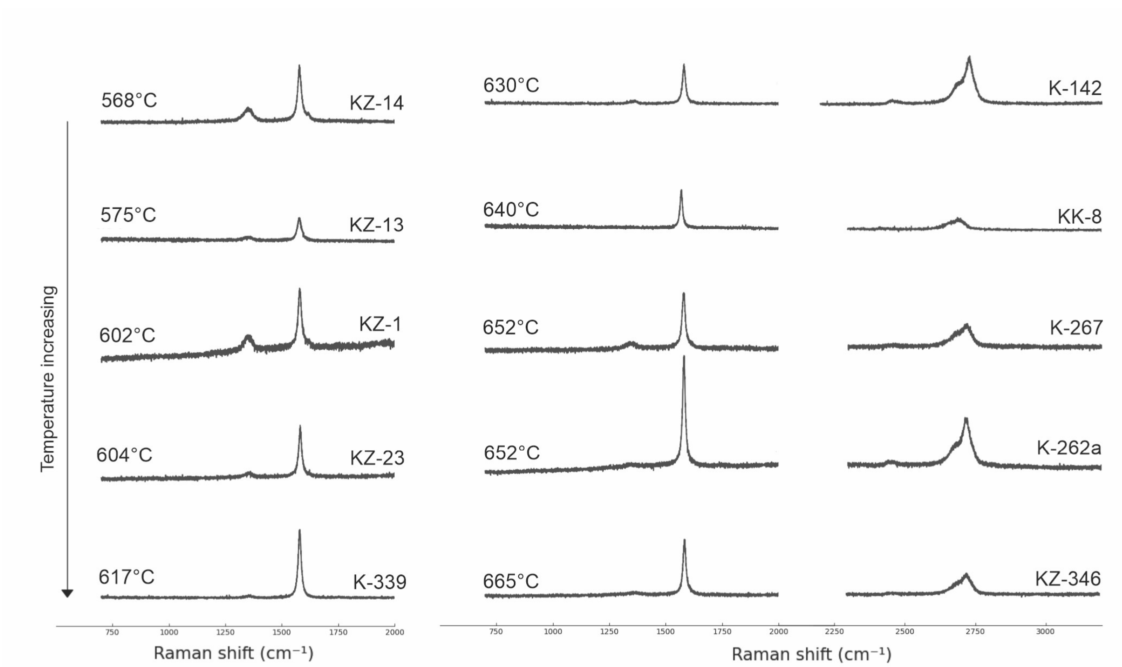

Figure 28: Representative Raman spectra of carbonaceous material of graphite-bearing metasediments with given temperature and sample name, respectively. The 1. order (750-2000 cm-1) and the 2. order (2250-3050 cm-1) are depicted.

To improve the reliability of RSCM analyses, 20 spectra per carbonaceous material (CM) sample were targeted. Covered or altered grains, luminescence effects, or significant spectral misfits led to a reduction in the number of processed spectra. For the 2. order, small and dispersed CM grains can affect the resulting RSCM temperatures by an apparent reduction of the actual structural order (see Rantitsch, 2023, for details). Due to this effect, 1. order spectra were fitted following the method of Lünsdorf et al. (2017), as presented in Table 2 for samples K-K-8, K-142, and K-339.

The provided band parameters G_STA, G_shape_factor, and S2_shape are included to illustrate the continuous evolution of CM and the quality of the RSCM temperature data (see detailed appendix). The analyzed samples fall within a temperature range of 568–665 °C.

Sample	Lithology	N	Temp [°C]	+/-	G_STA	std	G_shape_factor	std	S2_shape median	std
K-346	mica schist, Gr aggregates	16	**665**	25					1.4	0.5
K-262a	hornfels, Gr rich cracks	15	**652**	25					1.5	0.4
K-267	mica schist, Gr aggregates	17	**652**	25					1.5	0.8
K-K-8	Quartzitic mylonite, graphitic layers	20	**640**	31	15.3	2.6	12.5	4.2		
K-142	And Gr mica schist	15	**630**	31	16.9	1.9	16.5	2.5		
K-339	And Gr mica schist	15	**617**	31	18.9	2.0	14.8	3.6		
K-Z-23	phyllite, graphitic blasts	20	**604**	31	21.0	4.9	11.3	3.4		
K-Z-1	mica schist, graphitic	18	**602**	40	21.3	6.8	11.0	3.9		
K-Z-13	impure marble mylonite	20	**575**	31	25.8	5.7	10.5	2.5		
K-Z-14	graphite phyllite	20	**568**	31	27.0	3.2	7.5	1.7		

Table 2: Temperatures from the Raman spectra of carbonaceous material of graphite-bearing metasediments for the 1. order after Lünsdorf et al. (2017); G-STA=total area scaled by the G maximum intensity and the 2. Order after Rantitsch (2023).

5 Discussion

5.1. Contact aureole of the Kos pluton

The Miocene Kos monzonite exhibits an exposed surface of ~4 km in diameter (Triantaphyllis & Mavrides, 1998). The pluton penetrates the Marina Basement Unit, creating a contact aureole characterized by a proposed thermal gradient ranging from ~800 °C at the contact to ~500 °C outward (Altherr et al., 1976; Kalt et al., 1998). In contrast, the Marina Cover Unit remained unaffected by the monzonite intrusion nearby due to the presence of several W-E striking high-angle normal faults that juxtaposed these lithologies (Altherr et al., 1976; Roche et al., 2024; Van Hinsbergen & Boekhout, 2009). During the emplacement of the intrusion, contact metamorphic minerals in the Paleozoic metasediments were formed. In proximity to the contact, monzonite-hornfels metasomatism created skarn minerals like grossular, diopside-hedenbergite, and wollastonite. The clinopyroxene indicates an exsolution texture (Guy, 1980) in the thin section of KK-8.

Based on mineral assemblage and experimentally derived phase relations, Altherr et al. (1976) delineated isograds that define the extent of the ~4 km-wide contact aureole, extending across the Marina Basement Unit toward the Dikeos Unit in the east (Fig. 29). The work of Roche et al. (2024) questioned this assumption and highlights the thermometric calculations of Kalt et al. (1998) where the minimum temperature of the thermal overprint is reached within 1,258 m of the intrusion. Roche et al. (2024) proposed a revised model, limiting the thermal effect to a maximum distance of ~600 m at 500 °C, suggesting a limited metamorphic overprint.

This study generally concurs with the mineral paragenesis recorded, by Altherr et al. (1976) and Kalt et al. (1998), as well as the suggested isograds, as comparable assemblages were observed. Nevertheless, the index minerals diopside, sillimanite, and wollastonite occur exclusively near the intrusion, raising questions about the proposed thermal gradient and the dominance of thermal overprint. The occurrence of skeletal chiastolite in a quartz-mica schist (KZ-1) located ~2-3 km away from the pluton suggests a temperature-controlled metamorphism, as chiastolite formation is typically associated with contact metamorphosed pelitic rocks, though not exclusively (Mason et al., 2010 and references cited therein; Okrusch & Frimmel, 2022).

Since the monzonite intrusion of Kos is not unique, other Miocene plutons on Aegean islands like Lavrion, Ikaria, Serifos, Myconos, or Naxos (e.g. Altherr et al., 1988; Altherr & Siebel, 2002; Bolhar et al., 2010; Ducoux et al., n.d.; Stouraiti et al., 2010) have been extensively studied for correlation. There are striking similarities in the geochemical characteristics with monzonitic complexes of the island of Samos and the Bodrum peninsula (Mezger et al., 1985). Another comparable contact aureole occurs on Tinos, where a temperature range of ~475-660 °C, at ~3 kbar, within 600-2200 m to the Miocene granite body of ~5 km in diameter was stated (Bröcker & Franz, 1994). Consequently, the extent of the aureole of Kos is comparable to Tinos, but the distance deduced by Kalt et al. (1998) appears overestimated, given the uncertain subsurface geometry of the intrusion.

Hereby, the contact aureole is proposed to split into an inner aureole, depicting the pyroxene hornfels facies within tens of meters, which is characterized by the occurrence of fibrolite as well as metastable andalusite, clinopyroxene, and wollastonite. A middle aureole (~50 m - 1 km) that andalusite-cordierite hornfels and calcsilicate hornfels, representing the hornblende hornfels facies, and an outer aureole (~1 - 2.5 km), which is represented by Chl-Bt quartz schists and Gr-rich chiastolite schists. This outer aureole offers a greater temperature window to lower temperatures than described in Kalt et al. (1998), supporting a steeper temperature gradient consistent with Roche et al. (2024), where temperatures above 500 °C occur only within <600 m of the contact (Guy, 1980; Mason et al., 2010).

5.2. P-T Conditions of the Marina Basement Unit

To verify the existing temperature data and refine the understanding of the thermal gradient induced by the contact aureole, ten samples with a high carbonaceous content were analyzed by RSCM. The results are visualized alongside previously published temperature data (Kalt et al., 1998; Roche et al., 2024: Fig.29). The Na-in-cordierite thermometer (Mirwald, 1986) yields temperatures consistent with the proposed maximum temperature of 800 °C for orthopyroxene–hornblende coexistence (Altherr et al., 1976), but this is not corroborated by other geothermometers. Garnet–cordierite and garnet–biotite thermometers provide maximum temperatures of 686 °C (±50 °C) and 691 °C (±50 °C), respectively (Perchuk & Lavrent'eva, 1983), significantly lower than the Na-in-cordierite temperature of 762 °C (±18 °C). The latter is known to yield elevated values, likely due to incomplete equilibration, retrograde diffusion, or lower blocking temperatures for Fe-Mg exchange (Kalt et al., 1998).
This said, the gathered RSCM data (568-665 °C; +/-31° C) show a decent correlation with the mean temperature range of the garnet-cordierite thermometer (574-636°C; +/-50° C) and with the mean garnet-biotite thermometer (604-670°C; +/-50° C), considering uncertainties that the hot fluids introduce caused by fluid activity associated to the Miocene intrusion. It should also be noted that the extent of the intrusion is not defined and an expected temperature gradient in the contact aureole does not depict a perfect theoretical linear gradient, regardless of the

data set. Both new and published data indicate a relatively low gradient of ~100 °C, suggesting a possible baseline temperature of ~600 °C attributable to an earlier metamorphic event.

A possible solution is a regional metamorphic event in the amphibolite facies. On adjacent Dodecanes islands (Kalymnos, Leros and Lipsos) the basement rocks of the Panormos Unit experienced an overprint between 570 - 630 °C and 550 - 750 MPa (Franz et al., 2005). This correlates well with the afore-mentioned temperatures of the Marina Basement Unit. Although amphibole rim pressures of 313–506 MPa were initially calculated for Kos, these were later revised to ~200 MPa (Kalt et al., 1998). However, the noted pressure data could be relatable to regional metamorphism. While thermal overprinting by the pluton undoubtedly modified these values, they remain within the amphibolite-facies range, challenging a model of purely contact metamorphism.

The tectonic event responsible for the MP/MT base level and deformation of Paleozoic host rock is also supported by $^{40}Ar/^{39}Ar$ geochronology, indicating Variscan ages of 300-330 Ma (Roche et al., 2024). K-Ar dating on amphibole and muscovite from correlated basement rocks from Leros and Kalymnos yielded ages between 320 and 200 Ma (Franz et al., 2005; Grasemann et al., 2022).

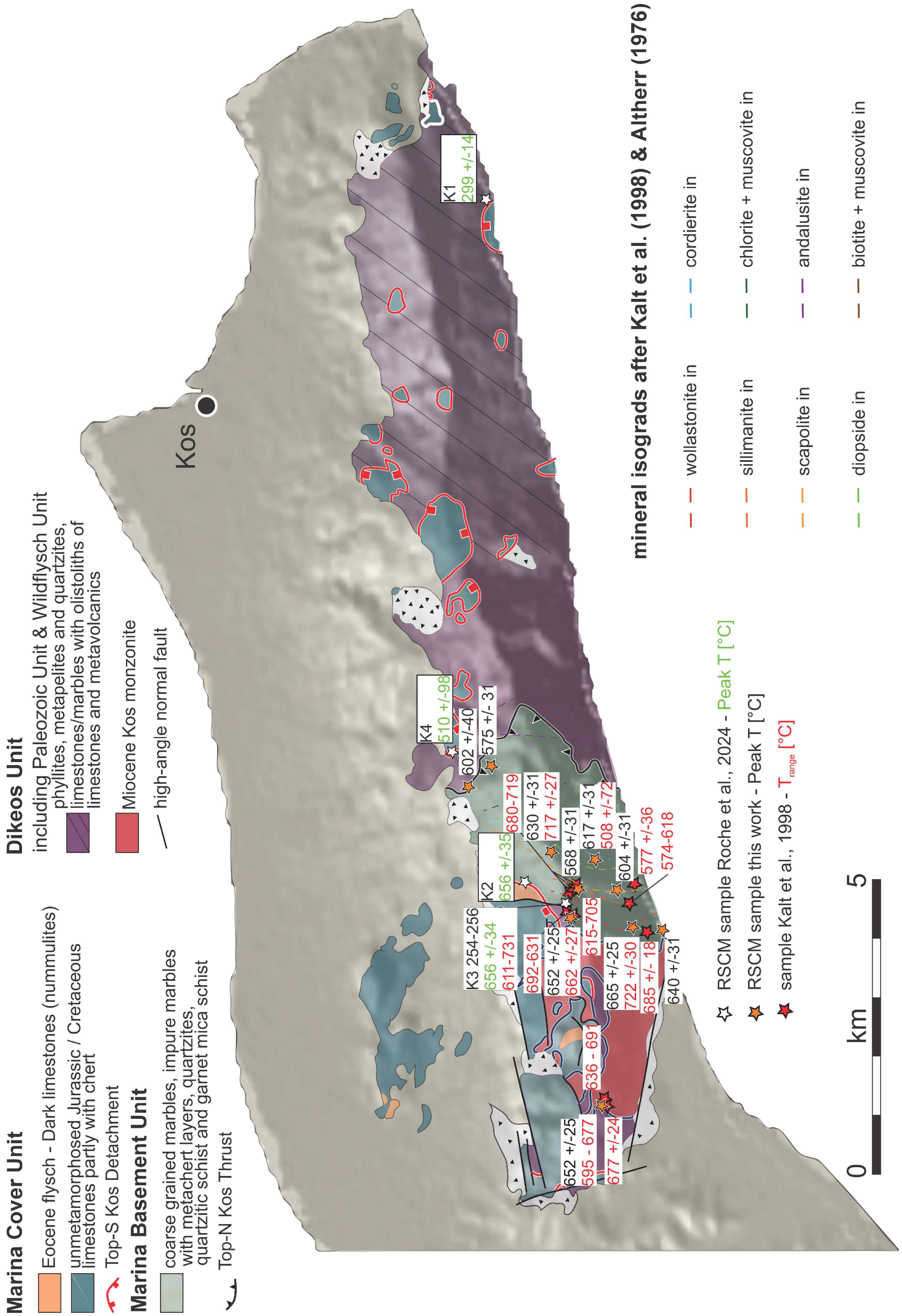

Figure 29: Geological map of Kos, modified after Roche et al. (2024) with isograds and temperature data from Kalt et. al. (1998) and RSCM temperature data from this work and from Roche et al. (2024).

5.3. Traces of a Variscan regional metamorphism

The lithology of the Marina Basement Unit comprises biotite or garnet mica schists, marbles. In proximity to the intrusion body, the host rock becomes a massive Hornfels. The foliation is overprinted by the temperature influx, resulting in chemical alternating layers controlled by precursor minerals (Fig. 8; Okrusch & Frimmel, 2022). Despite this thermal influence, the host rock shows deformation, intensity of which varies across the aureole. In the outer aureole, many samples exhibit a penetrative mylonitic fabric.

The Marina Basement Unit records polyphase deformation attributed to Variscan regional metamorphism under medium-temperature and medium-pressure (MT-MP) conditions (Franz et al., 2005; Roche et al., 2019). Notably, the Unit lacks any alpine metamorphic signature (Grasemann et al., 2022). At least three deformation phases are recognized, generating diverse fabric elements. A mylonitic foliation (S1) was deformed by a Type 2 and Type 3 refold interference pattern (Grasemann et al., 2004; Ramsay, 1962, 1967; Fig. 10). The refold structure is created by isoclinal folds (f1), which are aligned with the foliation and subsequently refolded by open cylindrical folds (f2). Cylindrical folds (f2) range from decimeter to meter scale, whereas isoclinal folds are restricted to centimeter or microscopic dimensions. Microstructural analysis reveals subgrain rotation (SGR) of the mineral fabric in all sections to a certain extent. Thin section KK-8 shows isoclinal fold cores defined by very fine blackish particles. This is attributed to the phenomenon called Zener drag, where a fine dispersed second phase impedes the migration of subgrains and grain boundaries; additionally, the recovery and recrystallization of grains from the matrix is restricted (Herwegh & Kunze, 2002 and references cited therein).

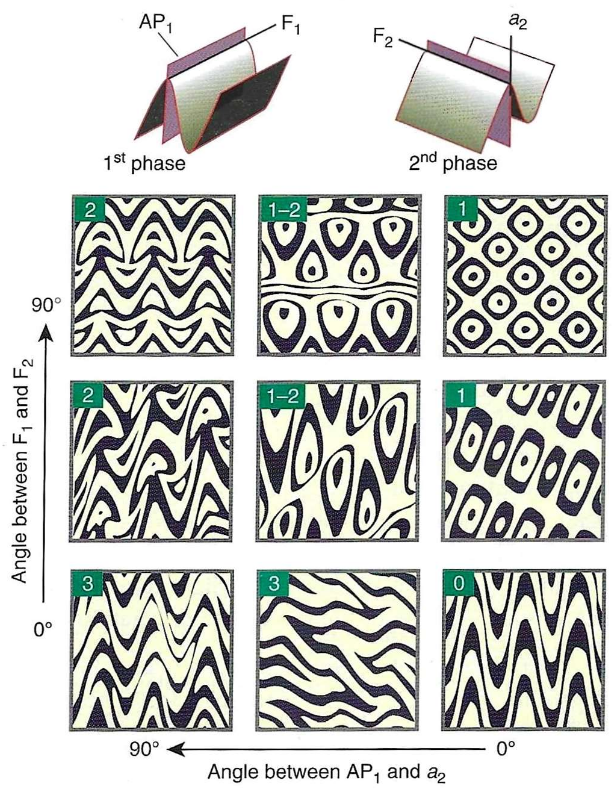

Figure 30: Possible fold interference patterns of cylindrical folds from Fossen (2016) after Ramsay (1967).

Although stretching lineation is difficult to discern due to fine-grained rocks and thermal overprint, numerous kinematic indicators are present. SCC′ structures at micro- and mesoscale indicate a shear sense top-to-NE. Asymmetric shear band boudinage aligned with foliation exhibits synthetic drag toward NNE (Passchier & Trouw, 2005). In phyllonites, competent layers of calcite or polycrystalline quartz display pinch-and-swell structures, some deformed by simple shear into sigmoids and weakly rotated winged inclusions (Grasemann & Dabrowski, 2015). Foliation occasionally hosts flanking fold structures as a crosscutting element (Grasemann & Stüwe, 2001; Passchier, 2001). In the case of the sample K-267 it is an a-type flanking fold with a normal drag (Grasemann et al., 2003).

Some samples show pressure solution cleavages like the Grt-biotite schist (KZ-9) or even more intense the And-Crd hornfels (KZ-18). They were picked up rather close to the Kos Thrust, which correlates with pressure solution cleavages described in the proximity of the Telendos Thrust on the adjacent islands of Kalymnos and Telendos (Grasemann et al., 2022). In the thin section of sample KZ-9, the cleavage structure, together with an enriched abundance of ilmenite is concentrated in the middle horizontal zone. This could reflect a predefined deformation horizon influenced by garnet porphyroblast rotation.

Kalt et al. (1998) focused on the mineral paragenesis of K-352, together with another sample and experimentally determined phase relations. Both were used to narrow down the P-T conditions. An absence of chlorite and presence of chloritoid together with cordierite, andalusite staurolite, and hercynite were described. (Kalt et al., 1998)

In contrast, thin section K-352 from this study exhibits a markedly different mineral assemblage (Fig. 24), underscoring lithological heterogeneity of the Unit. The fabric includes mylonitic foliation, isoclinal folding (f1), and a prominent kink band. The quartz-mica schist matrix comprises polygonal quartz with SPO and CPO, plagioclase, chlorite, amphibole, and accessory ilmenite and apatite, but lacks typical contact metamorphic minerals. The evidence of thermal overprint includes decussate chlorite textures and bulkier biotite with brownish interference colors concentrated in biotite–amphibole-rich layers. Pinch-and-swell structures of amphibole and quartz exhibit rotational components forming winged inclusions. The wing records SGR and is therefore a polycrystalline aggregate. The porosity of the rock sample is astonishing, displayed by many voids and fluid pathways and mix-phases along the grain boundary of quartz and plagioclase (Fig. 26; Mancktelow & Pennacchioni, 2004).

The intergrown aggregate of chlorite and ilmenite from observation site one (see chapter 4.2.3) may represent a former mica fish deformed to a mylonitic matrix of dynamically recrystallized quartz and plagioclase (Fig. 26.1 a&b). The elongated ilmenite needles, together with chlorite in three respective directions indicate a possible decomposition of biotite. The needles may follow a previous foliation or just decomposition defined by the former crystallographic lattice. At site three, another aggregate with decussate chlorite fibers is depicted. Compared to the other aggregate at spot one, ilmenite is absent, and apatite is enriched in the matrix, which wraps around the structure. Under CL, the aggregates exposes larger domains of plagioclases and quartz with lower gray values, depicting a sigmoid with a distinct tail (Fig. 26.3). Polygonal quartz and plagioclase phases underwent later thermal overprint (>500 °C), promoting grain-boundary area reduction (GBAR; Passchier & Trouw, 2005). In the strain shadows of the decomposed aggregates, decussate chlorite needles are predominant. At observation site two the CL-image reveals fractured detrital quartz clast relics aside of recrystallized quartz and plagioclase (Fig. 26.2).

All structures are influenced or overprinted by local deformation zones like the Kos Thrust or the Kos Detachment. These tectonic faults change the preexisting foliation and fabric elements, creating a Top-to-NNE shear sense close to the Kos Thrust on the northern slopes of the Dikeos mountain and a Top-to-SSW shear sense associated to the Kos Detachment.

5.4. Zoning of garnet and plagioclase

Garnets from eight thin sections exhibit diverse habits and compositions, notably the grossular-rich endoskarn of sample KK-1. This skarn contains amoeboidal grossular associated with pyroxene, plagioclase, and calcite, propagating into folded host rock. The matrix consists of quartz and plagioclase overprinted by pyroxene. Hydrogrossular occurs in the fold core, displaying oscillatory zoning typical of grossular-andradite garnets, and specifically for grossular from Kos (Fig. 15; Altherr et al., 1976; Vernon, 2018).

All other garnets form a porphyroblastic texture, where the garnet contains inclusions and fractures to varying degree. The large garnet porphyroblasts up to ~3 mm of KZ-9 have many helicitic quartz inclusions, whereas nearly idiomorphic garnets in KZ-10 and hypidiomorphic garnets in KK-3 and KK-4 are relatively pure, hosting only ilmenite, biotite, and quartz inclusions. The quartz inclusions sometimes appear as inclusion trails or are randomly distributed. Some garnets exhibit deflected foliation, strain shadows, or strain caps, consistent with intertectonic growth as noted by Roche et al. (2024). There are also the amoeboidal garnets of KZ-11, which reveal an extensive amount of ilmenite inclusions trails aligned with the matrix foliation. The high ilmenite content may reflect metasomatism linked to intrusion, supported by Ti-rich garnet types (melanite or schorlomite) in endoskarn and the homogeneous distribution of ilmenite near inclusion trails. However, an original Ti-rich protolith cannot be excluded. Garnets in KZ-18 occur as decomposed porphyroblastic relics with their reactant phases quartz and biotite.

To test if the iron-rich garnets record growth zoning or even reveal significant compositional changes, four profile lines were set from rim to core (Fig. 20&21). The first site is a garnet porphyroblast of KK-4 with an almost inclusion-free core and inclusion-rich rim area, indicating a two-phased growth (Roche et al., 2024). Another two garnets with an unusual core of ilmenite from sample KK-3, and one garnet domain from KZ-11 for comparison were analyzed. Despite the different appearances and optical differences based on the inclusion and various mineral assemblages, all profiles are broadly similar and reveal rather constant compositional parameters (Fig. 20&21). Although no profile line was set, the garnets in KZ-9 exhibit slight Fe enrichment at rims and Ca enrichment at cores, indicating weak compositional zoning. KK-11 has a significantly higher fraction of pyrope than the others, resulting in a different Mg-number (Fig. 21 b). Other almandines record Mg-numbers comparable to published data (Kalt et al., 1998). No major variation occurs in the Mn/Fe ration or in the $Fe^{2+}/(Fe^{2+}+Mg)$ ratio of garnet, which is 0.88, similar to the ratio of Franz et al. (2005). The FeO/(MgO+FeO) ratio for almandine-bearing mica schists is 0.96, exceeding the 0.8 reported by Altherr et al. (1976) for almandine–cordierite hornfels. Spessartine content is minor (~4%), contrasting with up to 50% in ‘nodular shales’ proposed by Altherr et al. (1976).

The Mg number decreases from rim to core, suggesting retrograde zoning. This trend correlates with the symplectitic structures of garnet with quartz and biotite as reactant phases, especially in previous strain shadows (Fig.14 a&b) and the decomposed garnet relicts of KZ-18. The garnet cores of the profile KK-3-1, KK-3-2 and KK-4 show slight Ca enrichment, indicating weak growth zoning. However, at temperatures >600 °C, compositional homogenization likely obliterates earlier zoning (Deer et al., 2013). Cathodoluminescence (CL) imaging of thin section K-352 reveals normal compositional zoning in plagioclase, with Na-rich rims and Ca-rich cores (Phemister, 1934; Fig. 26 b&d).

5.5. Tectonic evolution of the Marina Basement Unit

The tectonic history of the Paleozoic metasediments is suggested to be extended by a Variscan regional metamorphism, as indicated by geochronological data (Roche et al., 2024). Due to the small extent of the Marina Basement Unit, subsequent overprints of later events and the alteration of the rocks complicate mesoscale structural interpretation. Nonetheless, mineral paragenesis, petrological analysis, and the microstructural evidence point to amphibolite-facies P–T conditions during peak metamorphism. Following prograde deformation, symplectitic textures, decomposed porphyroblasts, and altered mineral assemblages indicate a retrograde evolution.

All previous structures are overprinted by the Eocene Kos top-to-N thrust and the Oligocene Top-to-S Kos Detachment (D. Papanikolaou & Nomikou, 1998; Roche et al., 2024). Both modify the fabric of the Marina Basement Unit, whereas the Kos Thrust dominates (Fig.11) on the northern slopes of Mount Dikeos, while the Kos Detachment has a weaker impact. During the Miocene, the monzonite intruded the Paleozoic sediments, producing a wide range of contact metamorphic minerals (Altherr et al., 1976; Kalt et al., 1998). Consequently, Mesozoic and Paleozoic rocks were disrupted by brittle Neogene W–E striking high-angle faults (Roche et al., 2024; Van Hinsbergen & Boekhout, 2009).

6 Conclusion

Structural and petrological investigations on the Marina Basement Unit on the island of Kos (Greece, Dodecanese) were conducted. Together with thermometric data in the contact aureole of the Miocene Kos intrusion, the influence of the aforementioned intrusion on the metasediments is discussed. Based on observations from outcrop to micro scale, this study provides new insights into the evolution and deformation history of the Marina Basement Unit.

The main findings can be summarized as follows:

1. The Miocene monzonitic intrusion exerted a strong thermal overprint on the Marina Basement Unit, forming a distinct contact aureole characterized by hornfels and skarn assemblages within the first tens of meters. High-temperature minerals such as andalusite, sillimanite, cordierite, and wollastonite confirm the localized nature of this metamorphism. Based on andalusite relicts the maximal extension was set to ~2,5 km.
2. Raman spectroscopy of carbonaceous material (RSCM) yielded peak temperatures between 568 °C and 665 °C, suggesting a baseline temperature of ~600 °C attributable to an earlier metamorphic event at amphibolite facies.
3. Outside the inner contact aureole, represented by the pyroxene hornfels facies, the metasediments preserve a well-defined mylonitic foliation, SGR and ductile shear sense indicators indicative of an earlier regional metamorphic event. Type 2 and Type 3 interference patterns, decomposed minerals, and pressure-dominated fabrics suggest a polyphase deformation history linked to Variscan regional metamorphism.
4. To reveal possible growth zoning, garnet porphyroblasts were analysed. The compositions are dominated by almandine with minor pyrope and spessartine components, while garnets of an endoskarn show significant grossular and andradite contents. Zoning profiles reveal limited chemical variation, suggesting that a thermal overprint may have eliminated potential growth zoning.
5. The Marina Basement Unit corresponds to the structurally lower Pelagonian rocks recording a complex deformation history. The geodynamic evolution of the Unit starts with a Variscan ductile deformation, causing refold interference patterns. During the Paleocene the Marina Basement Unit was thrust onto the Dikeos Unit (Kos Thrust) with top-to-N shear sense and later the Marina Cover Unit was juxtaposed onto the Dikeos Unit by the Oligocene Kos Detachment with top-to-S kinematics. The Miocene monzonite pluton penetrated the Marina Basement Unit, creating a contact aureole.

7 References

Allen, S. R., Stadlbauer, E., & Keller, J. (1999). Stratigraphy of the Kos Plateau Tuff: Product of a major Quaternary explosive rhyolitic eruption in the eastern Aegean, Greece. *International Journal of Earth Sciences*, *88*(1), 132–156. https://doi.org/10.1007/s005310050251

Altherr, R., Henjes-Kunst, F., Matthews, A., Friedrichsen, H., & Hansen, B. T. (1988). O-Sr isotopic variations in Miocene granitoids from the Aegean: Evidence for an origin by combined assimilation and fractional crystallization. *Contributions to Mineralogy and Petrology*, *100*(4), 528–541. https://doi.org/10.1007/BF00371381

Altherr, R., Keller, J., & Kott, K. (1976). Der jungtertiaere Monzonit von Kos und sein Kontakthof (Aegaeis, Griechenland). *Bulletin de La Société Géologique de France*, *S7-XVIII*(2), 403–412. https://doi.org/10.2113/gssgfbull.S7-XVIII.2.403

Altherr, R., Kreuzer, H., Wendt, I., Lenz, H., Wagner, G. A., Keller, J., Harre, W., & Höhndorf, A. (1982). *A late Oligocene/early Miocene high temperature belt in the Attic-Cycladic crystalline complex (SE Pelagonian, Greece)*. 97–164.

Altherr, R., & Siebel, W. (2002). I-type plutonism in a continental back-arc setting: Miocene granitoids and monzonites from the central Aegean Sea, Greece. *Contributions to Mineralogy and Petrology*, *143*(4), 397–415. https://doi.org/10.1007/s00410-002-0352-y

Bachmann, O., Allen, S. R., & Bouvet De Maisonneuve, C. (2019). The Kos–Nisyros–Yali Volcanic Field. *Elements*, *15*(3), 191–196. https://doi.org/10.2138/gselements.15.3.191

Blondeau, A., Fleury, J. J., & Guernet, C. (1975). Sur l'existence dans l'île de Kos (Dodécanèse, Grèce), d'une série néritique surmontée d'un flysch d'âge Cuisien supérieur ou Lutétien inférieur à sa base. *Comptes Rendus de l'Académie des Sciences de Paris*, *280*, 817–819.

Bolhar, R., Ring, U., & Allen, C. M. (2010). An integrated zircon geochronological and geochemical investigation into the Miocene plutonic evolution of the Cyclades, Aegean Sea, Greece: Part 1: Geochronology. *Contributions to Mineralogy and Petrology*, *160*(5), 719–742. https://doi.org/10.1007/s00410-010-0504-4

Bonneau, M. (1984). Correlation of the Hellenide nappes in the south-east Aegean and their tectonic reconstruction. *Geological Society, London, Special Publications*, *17*(1), 517–527. https://doi.org/10.1144/GSL.SP.1984.017.01.38

Bröcker, M., & Franz, L. (1994). The Contact Aureole on Tinos (Cyclades, Greece). Part I: Field Relationships, Petrography and P-T Conditions. *Chemie Der Erde*, *54*, 262–280.

Deer, W. A., Howie, R. A., & Zussmann, J. (2013). *An Introduction to the Rock-Forming Minerals (third edition)* (3rd ed.). Mineralogical Society of Great Britain and Ireland. https://doi.org/10.1180/DHZ

Desio, A. (1931). Le isole italiane d'll'Egeo. *Memorie Descrittive Della Carta Geologic' d'Italia, Roma*, 534.

Ducoux, M., Branquet, Y., Jolivet, L., Arbaret, L., Grasemann, B., Rabillard, A., Gumiaux, C., & Drufin, S. (2017). Synkinematic skarns and fluid drainage along detachments: The West Cycladic Detachment System on Serifos Island (Cyclades, Greece) and its related mineralization. *Tectonophysics*, v. 695, 1-26.

Dürr, St., & Jacobshagen, V. (1986). In *Geologie von Griechenland* (pp. 169–187). Gebrüder Borntraeger.

Franz, L., Okrusch, M., Seidel, E., & Kreuzer, H. (2005). Polymetamorphic evolution of pre-Alpidic basement relics in the external Hellenides, Greece. *Neues Jahrbuch Für Mineralogie - Abhandlungen*, *181*(2), 147–172. https://doi.org/10.1127/0077-7757/2005/0013

Grasemann, B., & Dabrowski, M. (2015). Winged inclusions: Pinch-and-swell objects during high-strain simple shear. *Journal of Structural Geology*, *70*, 78–94. https://doi.org/10.1016/j.jsg.2014.10.017

Grasemann, B., Schneider, D. A., Soukis, K., Roche, V., & Hubmann, B. (2022). Paleogeographic position of the central Dodecanese Islands, southeastern Greece: The push-pull of Pelagonia. *GSA Bulletin*, *134*(5–6), 1506–1528. https://doi.org/10.1130/B36095.1

Grasemann, B., & Stüwe, K. (2001). The development of Flanking folds during simple shear and their use as kinematic indicators. *Journal of Structural Geology*, 715–724.

Grasemann, B., Stüwe, K., & Vannay, J.-C. (2003). Sense and non-sense of shear in Fanking structures. *Journal of Structural Geology*.

Grasemann, B., Wiesmayr, G., Draganits, E., & Fusseis, F. (2004). Classification of Refold Structures. *The Journal of Geology*, *112*(1), 119–125. https://doi.org/10.1086/379696

Grew, E. S., Locock, A. J., Mills, S. J., Galuskina, I. O., Galuskin, E. V., & Halenius, U. (2013). Nomenclature of the garnet supergroup. *American Mineralogist*, *98*(4), 785–811. https://doi.org/10.2138/am.2013.4201

Guy, R. E. (1980). Virginia Polytechnic Institute and State University Blacksburg, Virginia. *Rocks & Minerals*, *55*(4), 158–161. https://doi.org/10.1080/00357529.1980.11764651

Henjes-Kunst, F., Altherr, R., Kreuzer, H., & Hansen, B. T. (1988). Disturbed U-Th-Pb systematics of young zircons and uranothorites: The case of the Miocene Aegean Granitoids (Greece). *Chemical Geology: Isotope Geoscience Section*, *73*(2), 125–145. https://doi.org/10.1016/0168-9622(88)90011-5

Henry, D. G., Jarvis, I., Gillmore, G., & Stephenson, M. (2019). Raman spectroscopy as a tool to determine the thermal maturity of organic matter: Application to sedimentary, metamorphic and structural geology. *Earth-Science Reviews*, *198*, 102936. https://doi.org/10.1016/j.earscirev.2019.102936

Herwegh, M., & Kunze, K. (2002). The influence of nano-scale second-phase particles on deformation of ®ne grained calcite mylonites. *Journal of Structural Geology*.

Jolivet, L., & Brun, J.-P. (2010). Cenozoic geodynamic evolution of the Aegean. *International Journal of Earth Sciences*, *99*(1), 109–138. https://doi.org/10.1007/s00531-008-0366-4

Kalt, A., Altherr, R., & Ludwig, T. (1998). *Contact Metamorphism in Pelitic Rocks on the Island of Kos (Greece, Eastern Aegean Sea): A Test for the Na-in-Cordierite Thermometer*. *39*(4).

Keller, J. (1969). Origin of rhyolites by anatectic melting of granitic crustal rocks: The example of rhyolitic pumice from the island of kos (agean sea). *Bulletin Volcanologique*, *33*(3), 942–959. https://doi.org/10.1007/BF02596758

Kokkalas, S., & Aydin, A. (2013). Is there a link between faulting and magmatism in the south-central Aegean Sea? *Geological Magazine*, *150*(2), 193–224. https://doi.org/10.1017/S0016756812000453

Lünsdorf, N. K. (2016). Raman spectroscopy of dispersed vitrinite—Methodical aspects and correlation with reflectance. *International Journal of Coal Geology*, *153*, 75–86. https://doi.org/10.1016/j.coal.2015.11.010

Lünsdorf, N. K., Dunkl, I., Schmidt, B. C., Rantitsch, G., & Von Eynatten, H. (2017). Towards a Higher Comparability of Geothermometric Data Obtained by Raman Spectroscopy of Carbonaceous Material. Part 2: A Revised Geothermometer. *Geostandards and Geoanalytical Research*, *41*(4), 593–612. https://doi.org/10.1111/ggr.12178

Lünsdorf, N. K., & Lünsdorf, J. O. (2016). Evaluating Raman spectra of carbonaceous matter by automated, iterative curve-fitting. *International Journal of Coal Geology*, *160–161*, 51–62. https://doi.org/10.1016/j.coal.2016.04.008

Mancktelow, N. S., & Pennacchioni, G. (2004). The influence of grain boundary fluids on the microstructure of quartz-feldspar mylonites. *Journal of Structural Geology*, *26*(1), 47–69. https://doi.org/10.1016/S0191-8141(03)00081-6

Mason, R., Burton, K. W., Yuan, Y., & She, Z. (2010). Chiastolite. *Gondwana Research*, *18*(1), 222–229. https://doi.org/10.1016/j.gr.2010.03.005

Mezger, K., Altherr, R., Okrusch, M., Henjes-Kunst, F., & Kreuzer, H. (1985). Genesis of acid/basic rock associations: A case study The Kallithea intrusive complex, Samos, Greece. *Contributions to Mineralogy and Petrology*, *90*(4), 353–366. https://doi.org/10.1007/BF00384714

Mirwald, P. W. (1986). Ist Cordierit ein Geothermometer. *Frotschritte Der Mineralogie*, *64*, 119.

Nemanich, R. J., & Solin, S. A. (1979). First- and second-order Raman scattering from finite-size crystals of graphite. *Physical Review B*, *20*(2), 392–401. https://doi.org/10.1103/PhysRevB.20.392

Okrusch, M., & Frimmel, H. E. (2022). *Mineralogie: Eine Einführung in die spezielle Mineralogie, Petrologie und Lagerstättenkunde*. Springer Berlin Heidelberg. https://doi.org/10.1007/978-3-662-64064-7

Papanikolaou, D. I. (2021). *The Geology of Greece*. Springer International Publishing. https://doi.org/10.1007/978-3-030-60731-9

Papanikolaou, D., & Nomikou, P. (1998). The Paleozoic of Kos: A low grade metamorphic unit of the basement of the external Hellenides terrane. *IGCP 276, Newsletter 6, Special Publications Geological Society of Greece*, *3*.

Passchier, C. W. (2001). Flanking structures. *Journal of Structural Geology*, *23*(6–7), 951–962. https://doi.org/10.1016/S0191-8141(00)00166-8

Passchier, C. W., & Trouw, R. A. J. (2005). *Microtectonics* (2nd ed.). Springer.

Pe-Piper, G., Piper, D. J. W., & Perissoratis, C. (2005). Neotectonics and the Kos Plateau Tuff eruption of 161 ka, South Aegean arc. *Journal of Volcanology and Geothermal Research*, *139*(3–4), 315–338. https://doi.org/10.1016/j.jvolgeores.2004.08.014

Perchuk, L., & Lavrent'eva, I. V. (1983). Experimental investigation of exchange equilibria in the system cordierite–garnet–biotite. In *Saxena, S. K. (ed.) Kinetics and Equilibrium in Mineral Reactions.* (pp. 199–239). Springer.

Phemister, J. (1934). Zoning in plagioclase felspar. *Mineralogical Magazine and Journal of the Mineralogical Society*, *23*(145), 541–555. https://doi.org/10.1180/minmag.1934.023.145.02

Ramsay, J. G. (1962). Interference Patterns Produced by the Superposition of Folds of Similar Type. *The Journal of Geology*, *70*(4), 466–481. https://doi.org/10.1086/626837

Ramsay, J. G. (1967). *Folding and Fracturing of Rocks*. McGraw-Hill.

Rantitsch, G. (2023). Graphite thermometry by interactive fitting of Raman spectra. *International Journal of Coal Geology*, *271*, 104232. https://doi.org/10.1016/j.coal.2023.104232

Rantitsch, G. (2024). Raman Spectroscopy of carbonaceous material thermometry in the Carnic Alps (Austria, Italy). *Austrian Journal of Earth Sciences*, *117*(1), 73–86. https://doi.org/10.17738/ajes.2024.0006

Rantitsch, G., Iglseder, C., Schuster, R., Hollinetz, M. S., Huet, B., & Werdenich, M. (2020). Organic metamorphism as a key for reconstructing tectonic processes: A case study from the Austroalpine unit (Eastern Alps). *International Journal of Earth Sciences*, *109*(6), 2235–2253. https://doi.org/10.1007/s00531-020-01897-7

Rantitsch, G., & Linner, M. (2021). Graphitization during high-grade metamorphism in the southern Bohemian Massif. *International Journal of Coal Geology*, *248*, 103864. https://doi.org/10.1016/j.coal.2021.103864

Reed, S. (2005). *Electron Microprobe Analysis and Scanning Electron Microscopy in Geology* (2nd ed.). Cambridge University Press. https://doi.org/10.1017/CBO9780511610561

Ring, U., Glodny, J., Will, T., & Thomson, S. (2010). The Hellenic Subduction System: High-Pressure Metamorphism, Exhumation, Normal Faulting, and Large-Scale Extension. *Annual Review of Earth and Planetary Sciences*, *38*(1), 45–76. https://doi.org/10.1146/annurev.earth.050708.170910

Roche, V., Grasemann, B., Schneider, D., Soukis, K., & Pichler, M. (2024). *Cold Tectonics of Kos, Central Dodecanese: Oligocene Bivergent Extension of the Pelagonian Domain*.

Roche, V., Jolivet, L., Papanikolaou, D., Bozkurt, E., Menant, A., & Rimmelé, G. (2019). Slab fragmentation beneath the Aegean/Anatolia transition zone: Insights from the tectonic and metamorphic evolution of the Eastern Aegean region. *Tectonophysics*, *754*, 101–129. https://doi.org/10.1016/j.tecto.2019.01.016

Rösler, H. J. (1979). *Lehrbuch der Mineralogie*. VEB Deutscher Verlag für Grundstoffindustrie.

Sadezky, A., Muckenhuber, H., Grothe, H., Niessner, R., & Pöschl, U. (2005). Raman microspectroscopy of soot and related carbonaceous materials: Spectral analysis and structural information. *Carbon*, *43*(8), 1731–1742. https://doi.org/10.1016/j.carbon.2005.02.018

Smith, P. E., York, D., Chen, Y., & Evensen, N. M. (1996). Single crystal^{40} Ar-^{39} Ar dating of a Late Quaternary paroxysm on Kos, Greece: Concordance of terrestrial and marine ages. *Geophysical Research Letters*, *23*(21), 3047–3050. https://doi.org/10.1029/96GL02759

Soder, C., Altherr, R., & Romer, R. L. (2016). Mantle Metasomatism at the Edge of a Retreating Subduction Zone: Late Neogene Lamprophyres from the Island of Kos, Greece. *Journal of Petrology*, *57*(9), 1705–1728. https://doi.org/10.1093/petrology/egw054

Stouraiti, C., Mitropoulos, P., Tarney, J., Barreiro, B., McGrath, A. M., & Baltatzis, E. (2010). Geochemistry and petrogenesis of late Miocene granitoids, Cyclades, southern Aegean: Nature of source components. *Lithos*, *114*(3–4), 337–352. https://doi.org/10.1016/j.lithos.2009.09.010

Triantaphyllis, M. B., & Mavrides, A. N. (1998). *Geological map of Greece: Eastern Kos Sheet* [Map]. Institute of Geology and Mineral Exploration (IGME).

Tuinstra, F., & Koenig, J. L. (1970). Raman Spectrum of Graphite. *The Journal of Chemical Physics*, *53*(3), 1126–1130. https://doi.org/10.1063/1.1674108

Van Hinsbergen, D. J. J., & Boekhout, F. (2009). Neogene brittle detachment faulting on Kos (E Greece): Implications for a southern break-away fault of the Menderes metamorphic core complex (western Turkey). *Geological Society, London, Special Publications*, *311*(1), 311–320. https://doi.org/10.1144/SP311.12

Vernon, R. H. (2018). *A Practical Guide to Rock Microstructure* (2nd ed.). Cambridge University Press. https://doi.org/10.1017/9781108654609

Warr, L. N. (2021). IMA–CNMNC approved mineral symbols. *Mineralogical Magazine*, *85*(3), 291–320. https://doi.org/10.1180/mgm.2021.43

Whitney, D. L., & Evans, B. W. (2010). Abbreviations for names of rock-forming minerals. *American Mineralogist*, *95*(1), 185–187. https://doi.org/10.2138/am.2010.3371

Willmann, R. (1983). *Neogen und jungtertiäre Entwicklung der Insel Kos (Ägäis, Griechenland)* (Stuttgart). *72*(3), 815–860.

8 List of Figures

9 List of Tables

10 Appendix

Sample	Lithology	Comment	Dip direction / Dip	Embedded / Loose	UTM_E	UTM_N
					35S	
KK-1	endoskarn	skarnfold / Grt+Px	-	loose	515429	4074386
KK-3	Grt-biotite schist	foldcore / Grt	-	embedded	516952	4074529
KK-4	Grt-biotite schist	foldcore / Grt	-	embedded	516952	4074529
KK-5	Grt-mica schist	foldcore / Grt / hercynite	282/68	embedded	517213	4074318
KK-6	Qz phyllonite	chiastolite relicts - spotted rock	-	embedded	517213	4074318
KK-7	Qz-mica mylonite	skarn (Cpx) - layer; SCC’ fabric	-	embedded	517353	4074360
KK-8	Quartzitic mylonite	skarn (Wo/Cpx) -layer; isoclinal folds	140/42	embedded	517353	4074360
KZ-1	Qz-mica schist	shear zone; chiastolithe relicts	-	embedded	519486	4078175
KZ-2	meta-marl	Chl + Amph	-	embedded	519486	4078175
KZ-3	Qz phyllonite	fold core; Amp, Chl, Qz	-	embedded	519514	4078170
KZ-3.1	meta-marl	Chl rich	308/36	embedded	519514	4078170
KZ-6	cataclasite	protholith: metapelite	-	embedded	517652	4076456
KZ-9	Grt-biotite schist	~2mm large Grt porphyroblasts	-	loose	517609	4076250
KZ-10	And-Crd hornfels	Grt, Crd, And porphyroblasts	-	loose	517609	4076250
KZ-11	Grt-Chl-Bt schist	Grt-porphyroblasts	-	loose	517609	4076250
KZ-12	Hbl hornfels	Amp, Scp, Pl	-	loose	517609	4076250
KZ-13	marble mylonite	impure; shearband boudinage	259/17	embedded	519870	4077802
KZ-14	Gr phyllonite	refold structure	-	loose	518512	4076584
KZ-16	calcite marble	minor organic / Gr components	230/25	embedded	517778	4076165

KZ-18	And-Crd hornfels	Scp, Crd, Grt, Pl, Bt; fold core	-	loose	517541	4076116
KZ-19	mica schist	Amp rich	-	loose	517541	4076116
KZ-21	And-hornfels	Chist porphyroblasts, graphite mica quartz matrix	-	loose	518443	4076266
KZ-22	phyllonite	refoldstructure, isoclinal fold; Amp	-	loose	518402	4075813
KZ-23	phyllonite	chiastolite relicts + Gr - spotted rock	200/12	embedded	517993	4075359
K-54	metavolcanite	-	-	loose	517541	4076116
K-142	And hornfels	chiastolithe	-	embedded	517927	4076036
K-143	Qz phyllonite	Chl-crack	-	loose	517843	4076174
K-151	calcite marble	calcite-coarse grains	-	embedded	517996	4076100
K-252	mica schist	Amp porphyroplasts	-	embedded	514344	4075139
K-262a	And-Crd hornfels	And, Sil/Fib, Pl, Qz, Bt; foliation	-	embedded	514230	4075172
K-267	biotite schist	asymmetric shear band boudinage, isoclinal folds, fault drag	-	loose	517476	4076124
K-339	And hornfels	chiastolite, Gr rich	-	embedded	518473	4075804
K-345	calcite marble	folds located in mica layers	-	embedded	517321	4074754
K-346	mica schist	Qz rich, folded, Gr aggregates	-	embedded	517381	4075013
K-352	Qz-mica myl	kinkband, isoclinal folds, winged inclusion, fault drag	-	embedded	517787	4075128
K-357	Qz-mica myl	Cal+Scp (swell) and Qz boudinage, SCC’ fabric	-	embedded	518136	4075078
K1			-		528483	4077772
K2			-		517957	4076993
K3			-		517662	4076223
K4			-		520012	4078506